

Guided Reinforcement Learning for Omnidirectional 3D Jumping in Quadruped Robots

Riccardo Bussola^{1,2}, Michele Focchi^{1,2}, Giulio Turrisi², Claudio Semini², Luigi Palopoli¹

Abstract—Jumping poses a significant challenge for quadruped robots, despite being crucial for many operational scenarios. While optimisation methods exist for controlling such motions, they are often time-consuming and demand extensive knowledge of robot and terrain parameters, making them less robust in real-world scenarios. Reinforcement learning (RL) is emerging as a viable alternative, yet conventional end-to-end approaches lack efficiency in terms of sample complexity, requiring extensive training in simulations, and predictability of the final motion, which makes it difficult to certify the safety of the final motion. To overcome these limitations, this paper introduces a novel guided reinforcement learning approach that leverages physical intuition for efficient and explainable jumping, by combining Bézier curves with a Uniformly Accelerated Rectilinear Motion (UARM) model. Extensive simulation and experimental results clearly demonstrate the advantages of our approach over existing alternatives.

Index Terms—Planning of Dynamic Motions, Reinforcement Learning, Legged Robots

Note: A supplementary video can be found at: (link). The code associated with this work can be found at: <https://github.com/mfocchi/orbit>.

I. INTRODUCTION

Quadruped robots are increasingly popular for their ability to move in very difficult terrains [1], often characterised by irregular slopes, gaps, and obstacles. This unique ability opens up a full range of possible missions, which are difficult or impossible for conventional robotic solutions (e.g., wheeled mobile robots) to execute. The flexibility of legged robots comes with a price: the complexity of their dynamic structure demands sophisticated solutions for motion control.

While controlling legged locomotion [2] is a relatively well-explored problem for walking and running manoeuvres [3], the difficulty of the problems grows significantly when the robot has to execute jumps longer than its legs size. This type of manoeuvre is often required in scenarios such as the exploration of hostile environments or for search and rescue in post-disaster management, where quadruped robots have a significant advantage over other platforms.

Unlike walking or running, which are based on continuous interaction between the feet and the ground and offer ample opportunities for frequent adjustments, jumping requires very precise control during the thrust phase to achieve the desired trajectory, since the robot cannot actively modify its trajectory

during the subsequent flight phase. The final phase, landing, demands stability and the ability to absorb impact forces averting damages to the robot's structure and preventing tipping over [4].

From a control perspective, the key challenges of jumping can be summarised in the following points:

- 1) **Optimisation of the thrust trajectory:** the desired lift-off state has to be reached while meeting dynamic constraints (e.g., joint position and velocity limits, and torque limitations).
- 2) **High-precision:** When the robot is airborne, its flight is governed solely by the conservation of momentum, as the robot is acted upon only by external forces. Therefore, the final landing point and configuration can deviate significantly in the case of even small trajectory tracking errors during the thrust phase.
- 3) **Strong real-time constraints:** The controller has to be executed in real-time as inputs need to be generated continuously and frequently during the entire jump, which is of limited duration.

These requirements, coupled with the complex nonlinear dynamics of the quadruped robots and the unmodelled effects of the interaction between feet and the ground, make control design a very difficult task.

A. Related work

The challenging problem of quadruped jumping has attracted a significant attention in the past few years, with many remarkable proposals in the literature.

A first group of researchers advocate the use of optimisation methods. A common solution to manage the complexity of the task is to employ reduced models, such as a 5-Degrees of Freedom (DoFs) representation of the quadruped's side view within the sagittal plane. This idea is often complemented by heuristic approaches that utilise physical intuition in the design of controllers or planners [5, 6]. While these hand-crafted motion strategies are grounded in physical reasoning, they often lack guarantees of physical feasibility. Another common approach involves whole-body numerical optimisation [7]. This method has led to spectacular results, such as the complex aerial manoeuvres performed by the MIT Mini Cheetah [8]. These manoeuvres include jumps, spins, flips, and barrel rolls, executed through a centroidal momentum-based nonlinear optimisation [9, 10, 11].

Despite the significance of these achievements, optimisation approaches are subject to well-known limitations. First, solving the nonlinear and nonconvex problem entails a very

¹ The authors are with the Dipartimento di Ingegneria and Scienza dell'Informazione (DISI), University of Trento. Email: name.surname@unitn.it

² The authors are with Dynamic Legged System (DLS), Istituto Italiano di Tecnologia (IIT), Email: name.surname@iit.it.

high computational cost, making this family of solutions difficult to deploy in real-time applications. Second, these approaches require detailed system models, which are challenging to construct on-the-fly in unstructured environments. The difficulty of accurately capturing dynamic contact timing, combined with the sparse nature of the control task (the controller operates only during the thrust phase), adds much to the complexity of the problem. Given these challenges, the application of traditional optimisation techniques [9, 10, 11] based on offline planning proves to be impractical, particularly for reactive approaches that demand frequent online replanning. An interesting way of addressing at least part of these problems can be found in the work of Song et al. [12], who propose an optimal motion planner that generates a variety of energy-optimal jumps. This is achieved by leveraging a library of pre-planned heuristic motions, which are automatically selected based on user-specified parameters or perception data. A different approach is the one proposed by Li et al. [13], who achieve barrel rolls using an Model Predictive Control (MPC) approach. This method gradually relaxes the planning problem along the prediction horizon—reducing model accuracy, coarsening time steps, and loosening constraints—to improve computational efficiency and performance. Ding et al. [14] leverage a SLIP template model to create 3D jumping motions.

In summary, in order to make MPC and optimisation-based methods computationally affordable, researchers frequently have to compromise on optimality, imposing artificial constraints [15, 7], such as pre-fixed contact sequences, prefixed flight-phase duration, or offline-optimised timing parameters. The price to pay can be high in terms of robustness: pre-specified foot contacts are known to create stability problems for a large mismatch between the expected and actual contact points [16]. The problem is being investigated. Bellegarda et al. [17] take inspiration from jumping frogs to reduce the number of parameters to a small set which can be optimised online to avoid the sim-to-real gap.

Advances in computational power, time-continuous action algorithms, and highly parallelised simulators have spurred interest in applying Reinforcement Learning (RL) to robot locomotion tasks. The pioneering work by Lillicrap et al. [18] demonstrated that actor-critic mechanisms combined with deep-Q networks can successfully learn policies in continuous action domains. Building on this fundamental result, RL has been applied to various quadruped locomotion tasks [19, 20, 21, 22, 23], including some early attempts at in-place hopping with legs [24]. Innovative parkour strategies, such as those proposed in [25], aim to extend the application of RL towards more dynamic motion patterns using purely End-to-End Reinforcement Learning (E2E) approaches.

E2E RL methods hold the promise to enable robotic jumping, but they typically require millions of training steps to converge on robust policies [26]. The primary difficulty stems from the sparse and non-smooth nature of the rewards. For jumping tasks, rewards are typically only provided after landing, and abrupt contact transitions create sharp discontinuities in the reward signal [27, 28]. The resulting learning process can turn out to be unstable and sample-inefficient. Additionally, RL policies often lack interpretability, complicating safety

validation and making it harder to ensure physical feasibility.

Several approaches address the issue of efficiency and robustness in RL training. For instance, combining trajectory optimisation (TO) with RL has been explored as a way to bootstrap policy learning and overcome issues of local optimality [29, 30, 31]. In these methods, RL is used to generate initial trajectories, thereby bootstrapping TO’s exploration process, avoiding local optima, and improving convergence.

The action space design is another crucial factor in RL efficiency and robustness [32, 33]. Some strategies consider using position or torque references [34] in joint [35] or Cartesian space to enhance learning. Shaffie et al. [36] further generalised RL policies across different quadruped morphologies by formulating both actions and observations in task space.

In order to achieve effective RL-based jumping strategies, Yang et al. [37] warm-start the policy by learning residual actions on top of a controller. This technique smooths the reward signal and improves convergence, but is limited to fixed-duration jumps. Vezzi et al. [38] employ a multi-stage learning approach, focusing on maximising jump height and distance, though with limited consideration for landing accuracy. Atanassov et al. [39] achieved remarkable results with a complex multi-stage training process and heavily engineered reward shaping. Although their work represents the state-of-the-art in RL-based jumping, the complexity of the approach may limit its general applicability. For this reason, we will use their work as a baseline to compare with the method proposed in this paper.

A comprehensive overview by Esser et al. [40] suggests that incorporating task-specific knowledge (known as Guided Reinforcement Learning (GRL)) is the most effective way to address the challenges posed by E2E in complex tasks. Along this line, [36] injects some domain knowledge into the training process, demonstrating that locomotion can be achieved by modulating an underlying Central Pattern Generator (CPG)-based motor-control scheme. In conclusion, while optimisation-based and RL methods have made significant progress in quadruped locomotion, there is still a clear gap in effective solutions for the quadruped jumping task, particularly in non-flat environments.

B. Contribution

This work proposes a GRL-based strategy for precise **3D omnidirectional quadruped jumping**. It is designed to plan the entire jumping action from standstill to elevated (or depressed) terrain in a few milliseconds, thereby enabling **real-time applications**. This is achieved by parametrising the jump trajectory in Cartesian space. This way we simplify the problem by modelling the jumping task as a **single action**, which addresses the sparsity inherent in conventional RL approaches.

The core idea is to exploit physical intuitions to model the jump trajectory. Our previous work on monopod jumping [41] provided valuable insights into using GRL to address the sparsity and complexity of linear jumping, forming the foundation for our quadruped jumping approach. That work

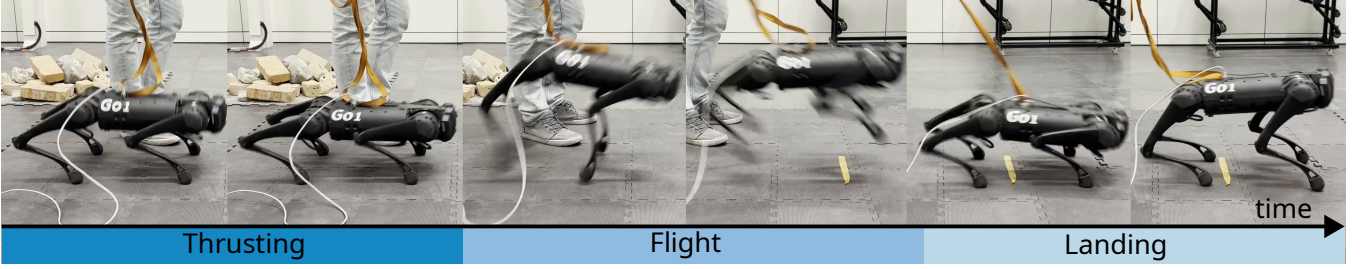


Fig. 1: Snapshots of Unitree Go1 robot executing the three stages of a jump: Thrusting, Flight, and Landing phases.

employed Bezier curves to parametrise the monopod’s Center of Mass (CoM) motion, concentrating learning within a small set of parameters. In this study, we build upon these results for the more complex quadruped scenario, introducing control over both the translational and angular dynamics. The latter was not included in the preparatory work on monopods.

Our simulation and experimental results show that this approach not only enhances accuracy and secures quick, robust convergence of the learning process, but also instils a high degree of reliability into the RL policy, ensuring safer and more dependable actions. For instance, given the lift-off configuration, we can utilise ballistic equations to make tight predictions on the landing position and timing. Unlike other methods requiring multi-stage learning or preliminary goal-specific tasks, ours is a *single-stage* learning process that directly achieves the final goal without intermediate training steps. This simplification improves sample efficiency and significantly impacts training time.

From a functional perspective, the integration of orientation and angular velocity allows us to exploit the robot’s full dynamic capabilities, optimising its orientation at take-off; additionally, controlling angular velocity enables the robot to adjust its pitch mid-air, reducing impact forces upon landing. Finally, this approach facilitates novel jump manoeuvres, such as in-place twist jumps, where the robot can rotate its body mid-air without linear displacement, expanding its repertoire of dynamic actions.

From an implementation standpoint, the method computes CoM references, which are then mapped to joint positions using Inverse Kinematic (IK). Planning the action in Cartesian space also renders the system adaptable to various quadruped morphologies (or even other legged robot morphologies, e.g., humanoids). The joint references are tracked by a low-level controller, leveraging the robustness of classical control methods to handle uncertainties in friction, masses and inertias. This alleviates issues arising from imprecise parameter knowledge, removing the need for extensive domain randomisation during training and making our method more robust and immune to overfitting. To summarise, the main contributions of our work are:

- A novel, sample-efficient RL method designed for quadruped robot omnidirectional jumping, which leverages the concept of **Guided Reinforcement Learning** to inject system knowledge into the task formulation.
- A formulation of an action-space for jumping tasks, which is: 1) robot-agnostic; 2) provides the possibility

to predict the outcome of the desired robot jump motion, enhancing the predictability of RL in such scenarios; and 3) can be used as an effective heuristic for predicting the jump apex and touch-down moments.

- A large set of simulation and experiments on two different quadrupeds (Aliengo and Go1) validating the method’s efficacy and repeatability. The learned policy is transferred from simulation to real robots, and its robustness is evaluated in simulation under varying damping and mass conditions. Compared to [39], our approach achieves a lower standard deviation in landing error and higher sample efficiency. For both simulation and real experiments, we also provide a statistical analysis of the accuracy.

C. Outline

In Section II we illustrate an overview of the proposed method, in Section III we define the adopted parametrization of the thrust trajectory, we illustrate in Section IV the Learning model used in our GRL approach. In Section V we report simulation and experimental results of omnidirectional jumps achieved with the Aliengo and Go1 robots, finally, in Section VI we draw the conclusions.

II. GUIDED REINFORCEMENT LEARNING

A. Jump Taxonomy

In this work, we have chosen to adopt a jumping technique known as pronking (or stotting), where all four legs push simultaneously on the ground, as seen in some mammals¹. This creates a single continuous thrust phase, enabling straightforward parametrization. Biomechanically, it consists of three phases: thrust, flight, and landing (see Fig. 1). **Thrust Phase:** it involves an initial compression followed by explosive decompression, akin to a spring release. An effective timing and an efficient energy management are crucial for optimising acceleration, flight duration, and landing. A proper force distribution prevents imbalances and ensures safe execution, considering terrain constraints such as friction.

Flight Phase Once airborne, the motion follows ballistic principles and is governed solely by gravity. Although thrust cannot be adjusted mid-flight, minor leg repositioning aids obstacle avoidance. Additionally, retracting legs mid-flight and extending them before touchdown optimises impact

¹The other jumping strategy is the leaping technique, in which the animal initially pushes the ground with all four legs. As it propels forward, it pitches its body up so that only the hind legs remain in contact with the ground, and the final push is executed by these remaining two legs.

absorption, as explained later. During the flight phase, no additional thrust is generated, making the jump trajectory entirely dependent on momentum generated at lift-off.

Landing Phase In this phase, ground contact is re-established while mitigating impact forces. The leg positioning from the flight phase is key to absorbing shocks and maintaining stability. A compliant landing strategy is beneficial to dissipate kinetic energy, preventing tipping and structural stress, and ensuring a smooth transition back to standing. To achieve safe landing, Roscia et al. [4] developed an optimisation-based Landing Controller (LC) using a Variable Height Springy Inverted Pendulum (VHSIP) model to manage flight and landing phases. The LC adjusts foot positions based on horizontal velocity during flight, ensuring stable landings without bouncing and slippage. While an LC significantly affects jump performance, we deliberately omitted it during both training and experiments to focus on the thrust phase—the most critical stage, as it determines the force needed to reach the target and ultimately dictates the jump’s success.

B. Method Overview

Since the landing position depends solely on the *lift-off* configuration, selecting this configuration appropriately is crucial for reaching the desired target. In this section, we analyse how the lift-off state influences the landing position, emphasising the inherent complexity of jump planning.

To simplify the problem, the robot flight phase is modeled as the projectile motion of a rigid body influenced only by gravity. In the absence of other external forces, this *ballistic* trajectory lies within the plane defined by the lift-off point and the target location. Consequently, planning a jump reduces to finding the inverse relationship between the desired target location c_{tg} and the corresponding lift-off configuration—comprising position c_{lo} and velocity \dot{c}_{lo} . Since the trajectory remains constrained to the plane tangential to both the initial and target positions, all feasible lift-off CoM positions and velocity vectors that result in the same target c_{tg} , lie on this planar manifold. Any lift-off velocity with a component outside this plane would, due to momentum conservation during the flight, lead to a different landing point.

The projectile motion of the system can be described by the following set of equations:

$$\begin{cases} c_{tg,x} = c_{lo,x} + \dot{c}_{lo,x}T_{fl} \\ c_{tg,y} = c_{lo,y} + \dot{c}_{lo,y}T_{fl} \\ c_{tg,z} = c_{lo,z} + \dot{c}_{lo,z}T_{fl} - \frac{1}{2}gT_{fl}^2 \end{cases} \quad (1)$$

where T_{fl} represents the duration of the flight phase, and g denotes the acceleration due to gravity. For the sake of simplicity, in this description we consider the execution of a forward jump, neglecting orientation. In view of the property just described, we can analyse the ballistic motion within a two-dimensional side-view space (see Fig. 2), involving the z -axis and x -axis (first and third equation in (1)). To investigate the impact of the lift-off linear velocity on the jump outcome, given a desired target position, we fix the lift-off position ($c_{lo,x}, c_{lo,z}$), and work out the flight time from the

first equation of (1) and replace in the third. Then, by simple algebraic manipulations, the vertical component of the lift-off velocity $\dot{c}_{lo,z}$ can be expressed as a function of the horizontal one $\dot{c}_{lo,x}$

$$\dot{c}_{lo,z} = \frac{c_{lo,z} - c_{tg,z}}{c_{tg,x} - c_{lo,x}} \dot{c}_{lo,x} + \frac{c_{tg,x} - c_{lo,x}}{2} g \frac{1}{\dot{c}_{lo,x}} \quad (2)$$

This hyperbolic relation tells us that an infinite set of solution pairs can be chosen: for instance, it is possible to jump with smaller horizontal velocity staying longer in the air (i.e. higher vertical velocity) or the opposite. Flight time decreases as horizontal lift-off velocity increases since a lower horizontal component requires greater vertical thrust, prolonging flight. Optimizing for minimal flight time requires maximising horizontal velocity; however, not all solutions are compatible with the robot’s physical limits, such as joint position, velocity, and torque limits, and with the constraints posed by the environment. Given these considerations, we can model the problem of generating the thrust phase in the following terms:

Problem Statement 1. *Synthesize a thrust phase that produces a lift-off state (i.e. CoM position and velocity) that: 1. satisfies (1), 2. copes with the potentially adverse conditions posed by the environment (i.e. contact stability, friction constraints), 3. satisfies the physical and actuation constraints.*

Including lift-off position as a decision variable adds complexity, making the problem highly non-convex and requiring Nonlinear Programming (NLP) solvers. This problem is typically addressed alongside trajectory planning during the thrust phase, but its complexity often requires artificial constraints like fixed thrust or flight times to reduce computational load. NLP solvers, while useful, are sensitive to initialization and prone to local minima, making them unsuitable for real-time jumping tasks. Instead, GRL offers an efficient alternative solution by treating the lift-off configuration as the primary action of our policy, as it is the crucial factor determining the overall jump outcome. We employ reinforcement learning to generate optimal thrust trajectories, which are executed by a low-level tracking controller. Since the trajectory can be parameterized and computed in advance, it enables fast execution through a lightweight neural network. During the jump, the low-level controller continuously tracks the planned motion, ensuring robustness and closed-loop stability.

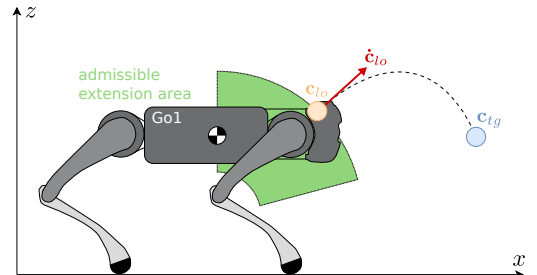


Fig. 2: Side-view of the ballistic problem.

Our approach is built on three key ideas. First, learning is conducted in Cartesian space, this design choice improves generalisation across different robot morphologies and configurations. Second, because the system follows ballistic dynamics during the airborne phase, the final landing position can be predicted *deterministically*. This allows the learning process to focus exclusively on the thrust phase—the moment when the robot propels itself off the ground and enables the integration of a *safety filter* (see Section V-B) that eliminates infeasible actions through simple computations. Third, inspired by biological systems, we guide the learning with prior knowledge about what a plausible motion should look like.

In mammals, movement patterns are shaped by evolutionary priors; similarly, we embed physical intuition into the learning process. A jump begins with a “charging” motion, during which the legs compress, followed by an explosive extension that accelerates the CoM upward and forward, generating momentum for lift-off. This charging motion aims to exploit the full joint range to produce acceleration.

Our key idea is to use a parametric curve to capture this motion, thereby enhancing and stabilising the learning process. Among the class of parametric curves suitable for this purpose, Bézier curves are particularly convenient due to their simple and efficient definition and computation. Notably, these curves offer two key advantages: their derivatives have simple expressions, and the curve lies entirely within the convex hull of its control points.

Using this representation, we apply an on-policy RL algorithm, Proximal Policy Optimization (PPO) [42], to learn the Bézier parameters (actions) by minimising cost functions similar to those used in optimal control.

Figure 3 illustrates our RL pipeline. The agent operates in either training or inference mode. During training, the Critic and Actor neural networks are periodically updated (as indicated by the dashed lines in the figure) once enough data has been gathered.

C. Control

To track a given CoM trajectory, we employ a kinematics-based approach combined with gravity compensation. IK is employed to compute the joint configurations and velocities that correspond to the given CoM trajectory. The computed joint positions $\mathbf{q}^d \in \mathbb{R}^n$ and velocities $\dot{\mathbf{q}}^d \in \mathbb{R}^n$ are then passed to a PD controller, along with a feedforward torque $\tau_{ff} \in \mathbb{R}^n$ derived from gravity compensation.

$$\begin{aligned} \tau &= \mathbf{K}_p(\mathbf{q}^d - \mathbf{q}) + \mathbf{K}_d(\dot{\mathbf{q}}^d - \dot{\mathbf{q}}) + \tau_{ff} \\ \tau_{ff} &= -\mathbf{J}_{cj}^T \underbrace{(\mathbf{J}_{cb}^T)^\dagger \mathbf{w}^g}_{\mathbf{f}_c} \end{aligned} \quad (3)$$

where $-\mathbf{J}_{cj}^T(\mathbf{J}_{cb}^T)^\dagger$ is the mapping of the gravity wrench $\mathbf{w}^g \in \mathbb{R}^6$ into joint torques and $\mathbf{f}_c \in \mathbb{R}^{3c}$ is the correspondent vector of feet forces, $n = 12$ is the number of actuated DoFs and $c = 4$ the number of contacts. We made the choice of using a sub-optimal simple control scheme instead of more elaborate ones to show the capability of the learning framework to compensate for controller inaccuracies.

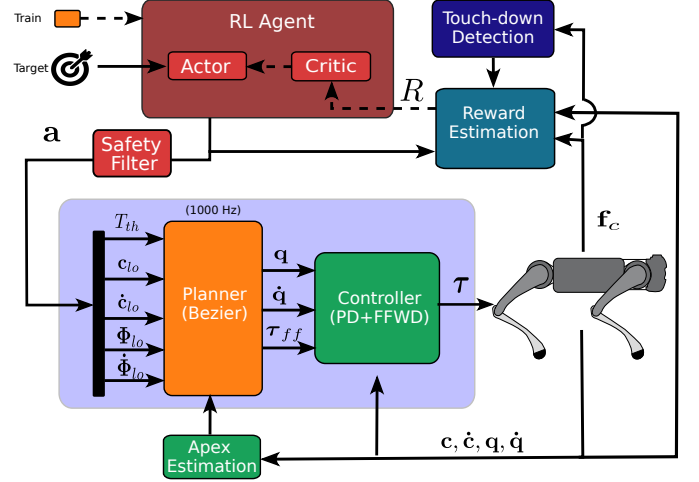


Fig. 3: Diagram of the GRL Framework. The framework is split into two levels: the RL agent and the planner. The RL agent produces an action for the planner based on a desired target. This computes a Bézier reference curve that is mapped into joint motion via inverse kinematics and tracked by the Proportional-Derivative (PD) controller that provides the joint torques to feed the robot. During the training, at the end of each episode, a reward is computed and fed back to the RL agent. Dashed lines are active when the framework is in training mode.

III. TRAJECTORY PARAMETRIZATION

A. Bézier Curves

Bézier curves are defined by a set of control points \mathbf{P} and constructed using Bernstein basis polynomials. The general formulation of a Bézier curve of degree n is as follows:

$$\begin{aligned} \mathbf{B}(t) &= \sum_{i=0}^n \binom{n}{i} t^i (1-t)^{n-i} \mathbf{P}_i \quad 0 \leq t \leq 1 \\ &= \sum_{i=0}^n \frac{n!}{i!(n-i)!} t^i (1-t)^{n-i} \mathbf{P}_i \\ &= \sum_{i=0}^n b_i^n(t) \mathbf{P}_i \end{aligned} \quad (4)$$

where n is the order of the curve, b_i^n is the Bernstein basis polynomial of degree n and $\mathbf{P}_i \in \mathbb{R}^3$ is the i^{th} control point. For a Bézier Curve of order n the number $\#\mathbf{P}$ of control points is equal to

$$\#\mathbf{P} = n + 1 \quad (5)$$

One of the most valuable properties of the Bézier curve is its differentiability, with its derivative also being a Bézier curve of order $n - 1$ (see Appendix A for details on the derivation)

$$\dot{\mathbf{B}}(t) = \sum_{i=0}^{n-1} b_i^{n-1}(t) \mathbf{P}'_i \quad 0 \leq t \leq 1 \quad (6)$$

with control points defined as

$$\mathbf{P}'_i = n(\mathbf{P}_{i+1} - \mathbf{P}_i) \quad (7)$$

The curve is originally defined over a normalized time interval $0 \leq t \leq 1$ but the formulation can be defined over arbitrary

time intervals $[0, T_{th}]$ with the following generalized form

$$\mathbf{B}(t) = \sum_{i=0}^n b_i^n \left(\frac{t}{T_{th}} \right) \mathbf{P}_i \quad 0 \leq t \leq T_{th} \quad (8)$$

It follows that, once the control points of a Bézier curve of order n are known, the control points of its derivative curve can be directly obtained

$$\begin{aligned} \mathbf{P}'_i &= \frac{n}{T_{th}} (\mathbf{P}_{i+1} - \mathbf{P}_i) \\ \dot{\mathbf{B}}(t) &= \sum_{i=0}^{n-1} b_i^{n-1} \left(\frac{t}{T_{th}} \right) \mathbf{P}'_i \quad 0 \leq t \leq T_{th} \end{aligned} \quad (9)$$

When selecting the order of the Bézier curve for our problem, we must consider the need to model both position and velocity. For any Bézier curve, the first and last control points correspond to the initial and final values of the curve. A third-order Bézier curve offers an ideal balance for modeling the position trajectory, as it provides four control points. The two intermediate control points can be used to shape the velocity profile, since all the four control points are later used to compute the derivative, and thereby the velocity trajectory. For the explicit form of the cubic Bézier curve and its derivative see Appendix B.

B. Jumping Strategy for quadrupeds

This work builds upon our previous work for a monopod [41] by including the angular dynamics, which has an impact on the distribution of contact forces, balance, and slippage, at the same time enabling dynamic maneuvers such as in-place twists for rapid reorientation.

The robot configuration is represented by the pair of vectors $(\mathbf{s}, \dot{\mathbf{s}})$, where \mathbf{s} includes the CoM position \mathbf{c} and trunk orientation Φ (expressed in ZYX Euler angles²), and $\dot{\mathbf{s}}$ includes the CoM linear velocity $\dot{\mathbf{c}}$ and trunk Euler Rates $\dot{\Phi}$. Additionally, we define the robot target configuration \mathbf{s}_{tg} as the vector containing the desired CoM position \mathbf{c}_{tg} and trunk orientation Φ_{tg} at *landing*. Starting from the explicit forms (38) of both the cubic Bézier curve and its quadratic derivative, we expressed the fulfillment of the boundary conditions as a linear system (10). Once solved, this system provides the control points of the thrust trajectory which links the initial state $(\mathbf{s}_0, \dot{\mathbf{s}}_0)$, to the lift-off state $(\mathbf{s}_{lo}, \dot{\mathbf{s}}_{lo})$:

$$\begin{cases} \mathbf{P}_0 = \mathbf{c}_0 \\ \mathbf{P}_3 = \mathbf{c}_{lo} \\ \mathbf{P}'_0 = \frac{3}{T_{th}} (\mathbf{P}_1 - \mathbf{P}_0) = \dot{\mathbf{c}}_0 \\ \mathbf{P}'_1 = \frac{3}{T_{th}} (\mathbf{P}_2 - \mathbf{P}_1) \\ \mathbf{P}'_2 = \frac{3}{T_{th}} (\mathbf{P}_3 - \mathbf{P}_2) = \dot{\mathbf{c}}_{lo} \end{cases} \quad \begin{cases} \mathbf{Q}_0 = \Phi_0 \\ \mathbf{Q}_3 = \Phi_{lo} \\ \mathbf{Q}'_0 = \frac{3}{T_{th}} (\mathbf{Q}_1 - \mathbf{Q}_0) = \dot{\Phi}_0 \\ \mathbf{Q}'_1 = \frac{3}{T_{th}} (\mathbf{Q}_2 - \mathbf{Q}_1) \\ \mathbf{Q}'_2 = \frac{3}{T_{th}} (\mathbf{Q}_3 - \mathbf{Q}_2) = \dot{\Phi}_{lo} \end{cases} \quad (10)$$

The only shared variable between the orientation and position trajectories is the thrusting time T_{th} , due to the duration constraints that both parameterizations must respect. Beyond this, the two trajectories remain completely independent. Including

an angular component enables regulation of the angular velocity at lift-off, making it possible to achieve landing postures that are more optimal in terms of Ground Reaction Forces (GRFs) distribution. In Fig. 4, the 3D visualization of a thrust trajectory for a simple forward jump is shown, both for the pure position parameterization and for the combined position and orientation parameterization, with a pitch derivative at lift-off of 4 rad/s.

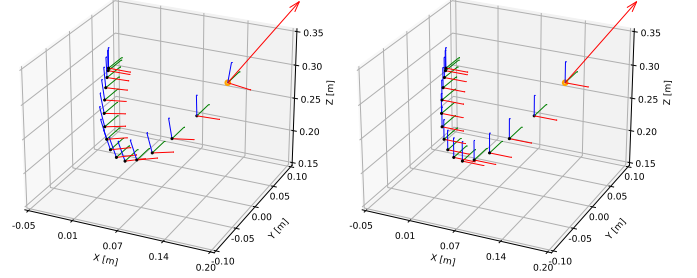


Fig. 4: 3D visualization of the thrust trajectory with (left) and without (right) angular motion.

C. Explosive Thrust

The Bézier-based parameterization (38) might limit the expressiveness of the thrust, particularly during the explosive decompression phase. According to the control point calculations in (10), for a given fixed thrust time, if we increase the lift-off velocity while keeping other boundary conditions unchanged, the control point \mathbf{P}_2 stretches the curve, resulting in a longer path to travel within the same timeframe. Certain lift-off velocities may need to be excluded from the feasible set, as the resulting trajectory could violate the robot's workspace constraints—for example, causing excessive squatting that would require an unfeasibly low height (i.e., the robot's belly would touch the ground, see Fig. 6). A promising solution to this issue is to split the trajectory in two parts where after the initial decompression stage, dictated by the Bezier, the path, in a second part, flattens to a straight line where the robot follows an Uniformly Accelerated Rectilinear Motion (UARM) (see Fig. 5). This would allow us to maintain

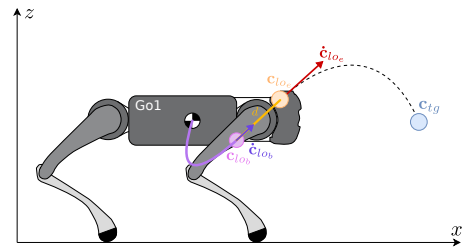


Fig. 5: Thrust trajectory with the new Bézier-UARM parametrization.

control over the thrust trajectory shape (i.e. do not result in workspace violations or unfeasible robot heights) while ensuring higher lift-off velocities. As explained later, this solution will introduce only a few additional parameters to

²It is reasonable to use Euler angle parametrization for the orientation during the thrust phase, despite the well known gimbal lock singularity issue at $\theta = \pi/2$ because we are not expecting such big orientation changes.

the *linear* part of the thrust trajectory, while the orientation remains unchanged. Let's outline the UARM equations of motion:

$$\begin{cases} v_f = v_0 + a(t - t_0) \\ d_f = \frac{1}{2}a(t - t_0)^2 + v_0(t - t_0) + d_0 \end{cases} \quad (11)$$

Where v_0 and v_f are the magnitudes of the initial and final velocities, d_0 and d_f are the initial and final displacements (on a line), and t_0 is the initial time. Solving for the time variable, setting $t_0 = 0$ for the sake of simplicity, after some manipulation we obtain the time term t and the acceleration term a :

$$\begin{cases} a = \frac{1}{2} \frac{v_f^2 - v_0^2}{d_f - d_0} \\ t = \frac{v_f - v_0}{a} \end{cases} \quad (12)$$

Previously, our thrust trajectory was characterized by the initial and lift-off CoM positions and linear velocities $(\mathbf{c}_0, \dot{\mathbf{c}}_0)$, $(\mathbf{c}_{lo}, \dot{\mathbf{c}}_{lo})$. Now, we introduce an intermediate configuration, $(\mathbf{c}_{lob}, \dot{\mathbf{c}}_{lob})$, which represents the endpoint of the Bézier parameterization and the starting point for the UARM trajectory. The actual lift-off configuration, will be the final condition of the UARM trajectory, now denoted as $(\mathbf{c}_{loe}, \dot{\mathbf{c}}_{loe})$. Given this new concept and notation, the system (12) becomes:

$$\begin{cases} a = \frac{1}{2} \frac{\|\dot{\mathbf{c}}_{loe}\|^2 - \|\dot{\mathbf{c}}_{lob}\|^2}{\|\mathbf{c}_{loe}\| - \|\mathbf{c}_{lob}\|} \\ T_{the} = \frac{\|\dot{\mathbf{c}}_{loe}\| - \|\dot{\mathbf{c}}_{lob}\|}{a} \end{cases} \quad (13)$$

Where T_{the} is the duration of the UARM part of the thrust trajectory. Renaming the duration of Bézier curve as T_{thb} , so the total thrust time becomes:

$$T_{th} = T_{thb} + T_{the} \quad (14)$$

Introducing the explosive lift-off configuration as additional parameters would involve adding six new variables, as $\dot{\mathbf{c}}_{loe} \in \mathbb{R}^3$ and $\mathbf{c}_{loe} \in \mathbb{R}^3$. However, such an increase would be inconveniently large. The properties of the Bézier curve can be

trajectory leveraging the UARM assumption. For example, the explosive lift-off velocity $(\dot{\mathbf{c}}_{loe})$ can be represented as a scaled version of the Bézier lift-off velocity vector $(\dot{\mathbf{c}}_{lob})$. Similarly, the total displacement of the explosive trajectory (\mathbf{c}_{loe}) can be expressed as an offset from the Bézier lift-off position (\mathbf{c}_{lob}) in the direction of the Bézier lift-off velocity. We introduce the velocity multiplier term k , so the explosive lift-off velocity is defined as:

$$\dot{\mathbf{c}}_{loe} = k\dot{\mathbf{c}}_{lob} \quad k \geq 1 \quad (15)$$

To compute \mathbf{c}_{loe} we first evaluate the unit vector based on the Bézier lift-off velocity to establish the direction of motion:

$$\hat{\mathbf{c}}_{lob} = \frac{\dot{\mathbf{c}}_{lob}}{\|\dot{\mathbf{c}}_{lob}\|} \quad (16)$$

Next, we introduce the displacement value d , allowing us to define the explosive lift-off position as:

$$\mathbf{c}_{loe} = \mathbf{c}_{lob} + d\hat{\mathbf{c}}_{lob} \quad d \geq 0 \quad (17)$$

By using this approach, only two parameters, k and d , are introduced instead of six, providing sufficient expressiveness without significantly increasing the problem's dimensionality. This formulation inherently ensures also that the explosive part is a direct continuation of the Bézier trajectory. The policy can still choose to exclude the contribution of the UARM phase for certain jumps by simply setting $d = 0$. Thus, the UARM trajectory can be defined as:

$$\text{uarm}(t) = \begin{cases} \mathbf{c}(t) = \text{lerp}\left(\mathbf{c}_{lob}, \mathbf{c}_{loe}, \frac{t - T_{thb}}{T_{the}}\right) \\ \dot{\mathbf{c}}(t) = \text{lerp}\left(\dot{\mathbf{c}}_{lob}, \dot{\mathbf{c}}_{loe}, \frac{t - T_{thb}}{T_{the}}\right) \end{cases} \quad T_{thb} \leq t \leq T_{th} \quad (18)$$

where lerp is a linear interpolating function, while, the Bézier position trajectory is expressed as:

$$\text{Position-Bézier}(t) = \begin{cases} \mathbf{c}(t) = \mathbf{B}_p\left(\frac{t}{T_{thb}}, \mathbf{P}\right) \\ \dot{\mathbf{c}}(t) = \dot{\mathbf{B}}_p\left(\frac{t}{T_{thb}}, \mathbf{P}\right) \end{cases} \quad 0 \leq t \leq T_{thb} \quad (19)$$

where the control points (10), using the new notation, are defined as:

TABLE I
Position-Bézier Control points

Position	Velocity
$\mathbf{P}_0 = \mathbf{c}_0$	$\mathbf{P}'_0 = \dot{\mathbf{c}}_0$
$\mathbf{P}_1 = \frac{T_{thb}}{3}\dot{\mathbf{c}}_0 + \mathbf{c}_0$	$\mathbf{P}'_1 = \frac{3}{T_{thb}}(\mathbf{P}_2 - \mathbf{P}_1)$
$\mathbf{P}_2 = -\frac{T_{thb}}{3}\dot{\mathbf{c}}_{lob} + \mathbf{c}_{lob}$	$\mathbf{P}'_2 = \dot{\mathbf{c}}_{lob}$
$\mathbf{P}_3 = \mathbf{c}_{lob}$	

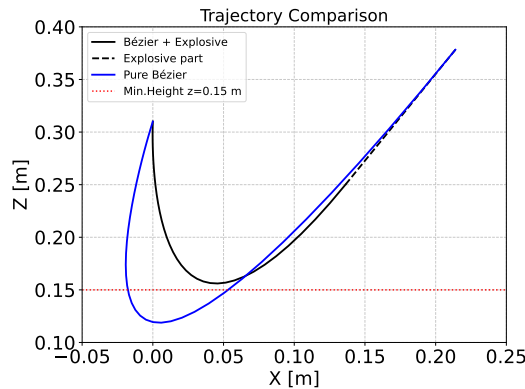


Fig. 6: Comparison of the two thrust trajectories computed using only Bézier (blue) and Bézier+Explosive thrust (black).

leveraged to define a reduced set of parameters for the jumping

Fig. 6 shows the two resulting trajectories: in black the new parameterization method, and in blue the previous pure Bézier one. In this example, a high final lift-off velocity with a magnitude of $3 \frac{m}{s}$ is required in both cases, with the same thrust time T_{th} . As illustrated, the previous parameterization

produces an unfeasible trajectory that violates the minimum height constraint of $z \geq 0.15$ m. This demonstrates that the new parameterization can generate explosive thrust trajectories while satisfying the system's feasibility constraints. For the orientation, instead, we employ the Bézier curve parametrization throughout the whole thrust duration T_{th} :

$$\text{Orientation-Bézier}(t) = \begin{cases} \Phi(t) = \mathbf{B}_o\left(\frac{t}{T_{th}}, \mathbf{Q}\right) \\ \dot{\Phi}(t) = \dot{\mathbf{B}}_o\left(\frac{t}{T_{th}}, \mathbf{Q}\right) \end{cases} \quad 0 \leq t \leq T_{th} \quad (20)$$

with control points defined as:

TABLE II
Orientation-Bézier Control points

Position	Velocity
$\mathbf{Q}_0 = \Phi_0$	$\mathbf{Q}'_0 = \dot{\Phi}_0$
$\mathbf{Q}_1 = \frac{T_{th}}{3} \dot{\Phi}_0 + \Phi_0$	$\mathbf{Q}'_1 = \frac{3}{T_{th}} (\mathbf{Q}_2 - \mathbf{Q}_1)$
$\mathbf{Q}_2 = -\frac{T_{th}}{3} \dot{\Phi}_{lo} + \Phi_{lo}$	$\mathbf{Q}'_2 = \dot{\Phi}_{lo}$
$\mathbf{Q}_3 = \Phi_{lo}$	

IV. LEARNING FRAMEWORK

The design of state and action spaces is crucial to ensure that a learned policy can be applied across robots with different morphologies. To achieve this, the state space should include only task-specific terms, such as the robot's centre of mass (COM) position and orientation, as well as the target position and orientation, while avoiding any joint-space information that would differ between robots. Mapping task-space information to joint space can be effectively handled by inverse kinematics (IK). This approach is complemented by the use of a low-level controller to ensure robust and accurate tracking performance, thereby enabling reusable policies across different robots [36].

A. The State

The state s_t is a representation of the environment at a specific time t and is fundamental for the policy to determine the appropriate action to perform. We define the state as the combination of the robot's current configuration (position + pose) and the desired configuration that we express as a displacement relative to the current (starting) position. In our setup, for simplicity, the robot always starts from a fixed joint configuration, meaning its initial position is constant. As a result, including this initial configuration in the state representation is redundant. Therefore, the state space can be more efficiently reformulated as:

$$\mathbf{s} = (\Delta \mathbf{c}, \Delta \Phi) \in \mathbb{R}^6 \quad (21)$$

Where $\Delta \mathbf{c} = \mathbf{c}_{tg} - \mathbf{c}_0$, $\Delta \Phi = \Phi_{tg} - \Phi_0$. This new state space directly captures the displacement command in both position and orientation, streamlining the policy's decision-making process.

B. The Action

The parameters of the thrust trajectory represent the action, i.e., the values that the policy must predict based on the input state. Considering the proposed thrust trajectory parameterization for position (18), (19), and orientation (20) the following parameters are required to compute the trajectory:

- T_{th_b} : the time interval in the thrust for which the initial Position-Bézier is used
- \mathbf{c}_{lo_b} : the lift-off position used for the Position-Bézier trajectory
- $\dot{\mathbf{c}}_{lo_b}$: the lift-off velocity used for the Position-Bézier trajectory
- \mathbf{c}_{lo_e} : the lift-off position used for the UARM trajectory, derived using the displacement term d
- $\dot{\mathbf{c}}_{lo_e}$: the lift-off velocity used for the UARM trajectory, derived using the velocity multiplier term k
- Φ_{lo} : the lift-off orientation used for the Orientation-Bézier trajectory
- $\dot{\Phi}_{lo}$: the lift-off Euler rates used for the Orientation-Bézier trajectory

Then, T_{th_e} is computed analytically via (13) and the total thrust time T_{th} is obtained by (14). The dimensionality of the action space is tightly related to the size of the exploration space and thus on learning performance. A smaller action space reduces the exploration area, simplifying the complexity of the mapping and speeding up the learning process. A trick to reduce the size of the action space is to express both the Bézier CoM lift-off position \mathbf{c}_{lo_b} and linear velocity $\dot{\mathbf{c}}_{lo_b}$ in *spherical coordinates*.

Due to the natural decoupling between linear and angular dynamics we treat the linear and angular motions separately. If no angular motion is present, due to the ballistic nature of the flight phase, the entire jump trajectory lies within the plane connecting the initial and target locations with the yaw angle φ_{jp} (which defines the orientation of the jumping plane in the $X - Y$ frame) remaining constant throughout the jump. This angle can be computed analytically from the initial and target positions restricting the coordinates of the lift-off configuration to a convex, two-dimensional space:

$$\begin{cases} \mathbf{c}_{lo_b,x} = r_p \cos(\theta_p) \cos(\bar{\varphi}) \\ \mathbf{c}_{lo_b,y} = r_p \cos(\theta_p) \sin(\bar{\varphi}) \\ \mathbf{c}_{lo_b,z} = r_p \sin(\theta_p) \end{cases} \quad \begin{cases} \dot{\mathbf{c}}_{lo_b,x} = r_v \cos(\theta_v) \cos(\bar{\varphi}) \\ \dot{\mathbf{c}}_{lo_b,y} = r_v \cos(\theta_v) \sin(\bar{\varphi}) \\ \dot{\mathbf{c}}_{lo_b,z} = r_v \sin(\theta_v) \end{cases} \quad (22)$$

As shown in Fig.7, the lift-off position \mathbf{c}_{lo_b} is defined by the extension radius r_p , pitch angle θ_p , and pre-computed yaw angle $\bar{\varphi}$. The lift-off velocity $\dot{\mathbf{c}}_{lo_b}$ shares the same yaw $\bar{\varphi}$ and is described by its magnitude r_v and pitch angle θ_v .

Given this, we can now define the action space, which encompasses both the position and angular components of the thrust trajectory, as follows:

$$\mathbf{a} = (T_{th_b}, r_p, \theta_p, r_v, \theta_v, k, d, \Phi_{lo,\psi}, \Phi_{lo,\theta}, \Phi_{lo,\varphi}, \dot{\Phi}_{lo,\psi}, \dot{\Phi}_{lo,\theta}, \dot{\Phi}_{lo,\varphi}) \in \mathbb{R}^{13} \quad (23)$$

The ranges of these values can be further constrained using domain knowledge to further narrow the search space. The thrust duration (T_{th}) must be short but sufficient for precise,

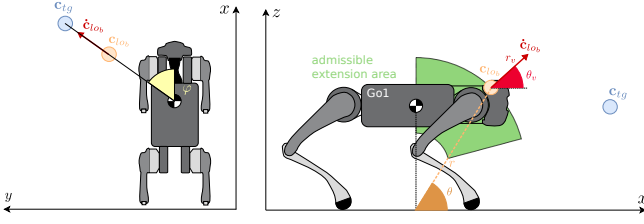


Fig. 7: Top and side views of the action in spherical coordinates for the quadruped robot

controlled lift-off; The radius r_p has to be smaller than a value r_{max} to prevent boundary singularity due to leg over-extension, and greater than a value r_{min} to avoid complete leg retraction. The bounds on the velocity \dot{c}_{lo} , represented by r_v and θ_v are set to rule out jumps that involve excessive foot slippage and useless force effort. Specifically, restricting $\theta_{v,min}$ to be positive ensures a non-negligible vertical component for the velocity, while bounding θ_v to the positive quadrant secures that the lift-off velocity will be oriented "toward" the target. The limits on lift-off roll/pitch/yaw angles (Φ_{lo}) limit the amount of possible re-orientation adjustments during the thrust to avoid losing stability and maneuverability, especially on uneven terrain; while the Euler rates ($\dot{\Phi}_{lo}$) at lift-off determine the reorientation of the robot during the subsequent flight phase; the Velocity Multiplier (k) amplifies thrust explosiveness, but must stay within trackable limits; the final displacement (d) adds travel distance and affects thrust phase duration. Given their physical meaning, we can impose specific ranges on these values (see Table V). Note that the above reductions, done at the level of action design, prevent the agent from exploring trajectories that are physically impossible, reducing the search space without any loss in terms of optimality.

C. A Physically Informative Reward Function

The reward function serves as the sole indicator that evaluates the effectiveness of an action in achieving the task goal. This comprises of a *physical* component which is a summation of penalties which is subtracted from a *target* component (positive) that assesses the achievement of the task's main objective: i.e. how closely the robot landed to the target location.

The core idea behind our reward design is that achieving the maximum reward related to the task goal requires adherence to and minimization of a set of physical system constraints. We have previously introduced the concept of path constraints, but to recap: a path constraint is a restriction that must be satisfied throughout the entire thrust phase. Any violation of these constraints results in a penalty. These path constraints are evaluated at each time step, and violations are penalized using the linear activation function $A(x, \underline{x}, \bar{x})$ defined in (24).

$$A(x, \underline{x}, \bar{x}) = |\min(x - \underline{x}, 0) + \max(x - \bar{x}, 0)| \quad (24)$$

All penalties are accumulated into a feasibility cost C_f . The set of path constraints, essential for ensuring the physical feasibility and safe execution of the jump, are evaluated at every time

step and include: joint position, velocity, and torque limits, friction cone, unilaterality, and staying away from singularity. By minimizing the penalties associated with any violations, the policy ensures that the robot operates in a physically feasible and reliable manner throughout the entire jump. However, path constraints are not sufficient to fully guide the policy towards optimal jump behavior. Additional costs are needed to promote desirable behaviors while penalizing unwanted actions. These costs differ from path constraints acting like behavioral "nudges" as they focus more on guiding specific behavior during the jump.

- **Lift-off tracking error (C_{lo}):** is the deviation between the reference and the actual twist at lift-off. This cost promotes the fact that the trajectory performed by the robot is accurately tracked by the low-level controller.
- **Target orientation error ($C_{\Phi_{tg}}$):** Instead of incorporating the orientation error in the positive reward, we treat it as a penalty. While the primary goal is to reach the target location, minimizing the orientation error at landing is crucial for task success because it enables to avoid catastrophic falls after touchdown.
- **Touchdown bounce penalization ($C_{\Delta x}$):** This regularization cost penalizes multiple bounces after landing, which can occur because we do not employ a sophisticated landing controller (e.g., as in [4]) and instead rely on simple joint impedance control. Excessive horizontal velocity at touchdown may lead to re-bouncing behavior before the robot comes to a complete stop, or even destabilize it, potentially causing a fall. To mitigate this, the cost is set to a high default value when no valid touchdown is detected - such as when the robot makes contact with the ground using body parts other than the feet. Otherwise, the cost is computed proportionally to the distance between the first detected touchdown and the robot's position at the end of the episode (timeout).
- **Touchdown angular velocity penalization ($C_{\dot{\Phi}_{td}}$):** This penalty discourages high angular velocities at touchdown, which could cause the robot to lose balance or suffer mechanical damage, leading to a failed jump.
- **Action limit penalization (C_{ppo}):** Differently from other RL algorithms that bound the action range to $[-1, 1]$, thanks to a tanh layer, the PPO algorithm computes actions by sampling from a normal distribution $a \sim \mathcal{N}(\mu, \sigma^2)$, which is not inherently constrained. To prevent actions from exceeding the defined range, clipping is introduced. Although this operation does not compromise the mathematical formulation of PPO, the choice of clipping range significantly impacts policy performance [43]. Therefore, determining the appropriate clipping range for PPO becomes an important hyperparameter (see Table IV). The C_{ppo} penalty informs the policy when an action exceeds the predefined bounds, thereby helping the policy to stay within the safe and feasible range.

These additional costs guide the policy towards safer, more stable, and physically feasible jump execution, further refining the policy's behavior during training. Regarding the positive reward task, we refer to it as the *landing target reward*

function, denoted by R_{lt} . This term measures how close the final landing location (evaluated at the episode's timeout) is to the target location. In this term, we also want to weigh errors differently depending on the jumping magnitude. The goal is to better distinguish the impact of landing errors e_{tg} based on the jump distance Δc . For example, an error of 0.2 meters is significant for a 0.1 meter-long jump but less severe for a 1 meter jump. Therefore, for a given distance error, the reward should increase proportionally with the desired jump distance. The revised landing target reward function is defined as follows:

$$R_{lt} = 1_{\mathbb{R}^+} \left[\exp \left(-\frac{e_{tg}}{\sigma_e} \right) \exp \left(\frac{\Delta c}{\sigma_d} \right) \right] \quad (25)$$

with

$$e_{tg} = \|\mathbf{c}_{tg} - \mathbf{c}\| \quad \Delta c = \|\mathbf{c}_{tg} - \mathbf{c}_0\|$$

where σ_e is a hyperparameter scaling the influence of the landing error, and σ_d the contribution of the jump distance. The first negative exponential achieves its maximum for zero landing error and rewards *accuracy* while the second (positive exponential) amplifies the previous factor according to the jump difficulty (i.e. to the same error is associated a higher reward if the jump distance is higher). This formulation makes the reward sensitive to both the landing error and the magnitude of the jump, ensuring that the policy is encouraged to perform well across different jump distances. In Fig. 8, the surface plot of this reward function is depicted. As can be observed, the reward increases as the landing error approaches zero. Furthermore, for the same landing error, the reward value increases proportionally with the desired jump distance, reflecting the relative importance of accuracy across different distances. Finally, the total reward function is [39]:

$$R = R_{lt}(\mathbf{c}, \mathbf{c}_0, \mathbf{c}_{tg}) e^{-(\sum C_{f,i})^2} \quad (26)$$

In this formulation, the reward remains positive and is dynamically scaled based on the penalty costs. As the sum of penalties increases, the negative exponent drives the reward toward zero, effectively suppressing any positive contribution. Conversely, when penalties are minimal, the exponential term

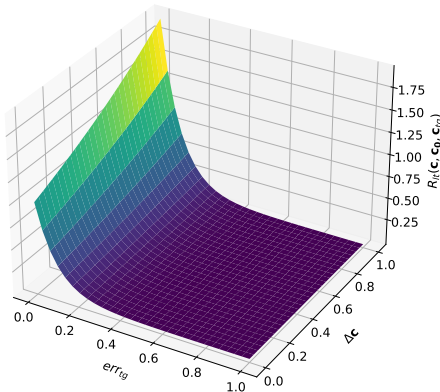


Fig. 8: Landing target reward function surface function of landing error and jump distance.

approaches one, preserving the full value of the landing target reward. This design keeps the reward function informative across the learning process, fostering better convergence and policy performance. To maximize the reward, the policy must minimize the cost penalties, thereby ensuring that all system constraints are respected. This guarantees that the proposed trajectory is both feasible and trackable, enabling the robot to perform optimal jumps within its physical limitations, ensuring safe and efficient deployment of the learned behaviors in real-world scenarios.

V. RESULTS

A. Simulation Setup

In this section, we present the results of our work, validated through simulation-based evaluation of the learned policy. We report the hardware specifications, as they critically affect training time and parallelization performance. Training and evaluation were performed on a desktop with an Nvidia RTX 3060 GPU with 12 GB of VRAM. The policy was trained using a modified version of the Orbit framework [44] compatible with our RL loop, leveraging parallel simulation of 4096 robots. The training has been performed both for the Go1 and the Aliengo, but, henceforth, we will detail the results solely for the Go1 robot. The robot controller and simulator parameters are detailed in Table III, while the hyperparameters used in the training are listed in Table IV. Table V specifies the ranges of action parameters defined from physical intuition with the aim to further restrict the search space. The learning episode starts from the same initial default

TABLE III
Go1 Robot and Simulator parameters

Variable	Name	Range
m	Robot Mass [kg]	13
P	Proportional gain	50
D	Derivative gain	0.8
\mathbf{q}_0	Nominal configuration [rad]	[0 -0.75 1.5]
dT	Simulator time step [s]	0.001
τ_{max}	Max Joint torque [Nm]	[23.7 23.7 35.5]
\dot{q}_{max}	Max Joint vel. [m/s]	[20 20 30]

configuration \mathbf{q}_0 continues until a timeout, requiring the robot to regain balance and return to a nominal state after landing. To maintain a unified control strategy, we decided not to include the LC as part of the simulation in the training phase, relying on a simplified impedance strategy. During the thrust phase, a default joint stiffness is set in the PD controller plus a Whole Body Control (WBC) for gravity compensation. Since all four feet are in contact with the ground throughout the thrust phase, the control strategy tracks the desired Cartesian trajectory and compensates for gravity. Contact is maintained by ensuring the fulfillment of both the friction cone and unilateral constraints during training. After thrust, the stiffness is reduced, the WBC is disabled, and the legs are retracted until the jump apex. After that, the legs extend back to the default configuration. Finally, upon touchdown, WBC is reactivated to compensate for gravity. To prevent torque discontinuities during configuration changes in the airborne phase, Cubic

TABLE IV
PPO hyper-parameters

Name	Value
Episode timeout	1.5s
Initial noise std	1.0
Network dimension	[512,256,128]
Activation layer	ELU
PPO Clip	0.2
Entropy coefficient	0.01
Number of learning epochs	10
Learning rate	1e-3
Gamma	0.99
Lam	0.95
Desired KL	0.01

TABLE V
Ranges of action parameters

Variable	Name	Range
T_{thb}	Time of Bezier thrust [s]	[0.4, 1.0]
r_p	Extension radius of Bezier thrust[m]	[0.2, 0.4]
θ_p	Position Pitch angle of Bezier thrust[rad]	$[\pi/4, \pi/2]$
r_v	CoM Velocity magnitude of Bezier thrust [m/s]	[0.5, 5]
θ_p	CoM Velocity Pitch angle of Bezier thrust [rad]	$[-\pi/6, \pi/2]$
k	Velocity multiplier for explosive thrust	[1,3]
d	Position displacement for explosive thrust	[0,0.3]
$\Phi_{lo,\psi}$	The pitch angle at lift-off	$[-\pi/6, \pi/6]$
$\Phi_{lo,\theta}$	The roll angle at lift-off	$[-\pi/6, \pi/6]$
$\Phi_{lo,\varphi}$	The yaw angle at lift-off	$[-\pi/4, \pi/4]$
$\dot{\Phi}_{lo,\psi}$	The angular velocity around the roll axis	[-1,1]
$\dot{\Phi}_{lo,\theta}$	The angular velocity around the pitch axis	[-1,1]
$\dot{\Phi}_{lo,\varphi}$	The angular velocity around the yaw axis	[-4, 4]

Hermite Spline Interpolation is used to smoothly transition joint references between extended and retracted configurations. In a future extension of this work, we plan to also introduce a separate Neural Network (NN) trained using an E2E approach, specifically tasked to adjust the joint configuration at each time step emulating a LC. For each completed episode, one PPO training step is performed, amounting to a total of 2000 training steps. Training the policy under this setup took approximately 15 hours. However, it's important to emphasize the sample efficiency of our approach when compared to typical E2E methods, such as those available in the Orbit framework. These methods generally require the recorded data of 20 to 25 simulation steps to complete a single training step. In contrast, our method performs a training step with just one env step, corresponding to the entirety of the episode since the episode is composed of only one action. This means that, given an equivalent number of policy training steps, our approach uses 20 times less data, highlighting the remarkable sample efficiency of the proposed framework, despite the training time is comparable (the overhead due to the simulation of the robots will be the same).

We define the training region for the policy as a cuboid space with the X-axis ranging from -0.6 to 1.2 meters, the Y-axis from -0.6 to 0.6 meters, and the Z-axis from -0.4 meters to 0.4 meters, allowing jumps up to 40 cm elevation. This setup ensures learning omnidirectional jumps to both elevated and depressed targets, providing a broad exploration of pos-

sible landing configurations. For the angular component, the training region is limited to a maximum of 15 degrees for roll and pitch, ensuring the robot can handle minor tilts during the jump. However, the yaw angle, which is of greater importance in this work, is allowed to vary significantly, covering a range from -90 to 90 degrees. This range ensures the policy can perform jumps with diverse orientations, preparing the robot for more dynamic scenarios.

In Fig. 9, we present both the total reward curve and the cumulative penalty sums for each training step. The total reward (upper plot) converges after only 2000 training steps. A crucial observation is the even faster convergence (after 250 episodes) of the cumulative penalties (lower plot) to a small value, suggesting that the learned policy quickly adapts to producing physically feasible actions and adheres to system constraints. This serves as strong evidence that our reward formulation is effective, driving the policy towards solutions that satisfy the constraints while optimizing the task's objectives.

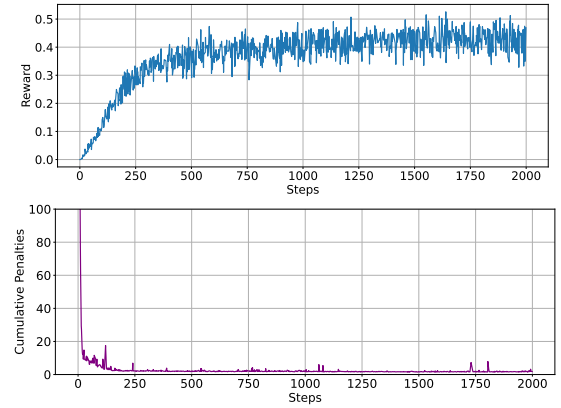


Fig. 9: Training curves over training episodes for the Go1 robot: total reward (top) and cumulative penalties (bottom), highlighting the policy's improvement and its adherence to physical constraints.

B. Physical feasibility check

The physically informed nature of our action enables us to perform a safety check on the action proposed by the RL policy, adding a certain level of explainability with respect to fully data-driven approaches. This feasibility check can be employed as an “a posteriori” safety feature in the *inference* phase, to check if a predicted action will lead to unsafe results. For instance, if the given CoM vertical velocity is not sufficient to reach the target height, the action will not produce a physically meaningful jump. This can be computed by obtaining the time to reach the apex $T_{f,up} = \dot{c}_{lo,z}/g$ and substituting it in the ballistic equation:

$$\bar{c}_z(T_{f,up}) = c_{lo,z} + \dot{c}_{lo,z}T_{f,up} + \frac{1}{2}(-g)T_{f,up}^2 \quad (27)$$

This results in $\bar{c}_z(T_{f,up}) = c_{lo,z} + \frac{1}{2}\frac{\dot{c}_{lo,z}^2}{g}$, which is the *apex* elevation. If $c_{tg,z} > \bar{c}_z(T_{f,up})$, the action can be aborted early without performing the jump, and high-level strategies could be adopted to relax the jumping requirements (e.g., lower the target height). This mechanism enhances safety and reliability

by preventing the execution of jumps that could lead to failures or unsafe outcomes.

C. Validation of Omnidirectional Jumps

In this section, we evaluate the performance of the learned policy in executing omnidirectional jumps on elevated/depressed terrains as well as its effectiveness in controlling orientation during dynamic jumps. The ability to jump in multiple directions, combined with the capability to adapt to varying surface heights, enhances the system’s versatility for real-world scenarios, where simple, single-direction jumps or fixed-height landings are often insufficient. Specifically, this validation will encompass forward, backward, and lateral jumps, as well as involving upward or downward motions on/from uneven surfaces. Rapid in-place/composite jumps involving yaw rotations will also be assessed. Through this validation, we aim to show the policy’s precision in reaching target positions and orientations. All the simulations have been performed for the Unitree Go1 robot.

1) *Flat Jumps and Feasible Region:* For this evaluation, we conducted 8192 jumps at various target positions, all with zero height displacement (flat jumps). The targets are sampled from the previously established training region, providing a comprehensive evaluation of the learned policy. The concept of the feasible region refers to the maximum area in which the robot can perform jumps while keeping the landing error below a specified threshold [41]. The absolute landing error (i.e. the distance between the *actual* landing position and the intended target) was calculated for each sample. Jumps were classified as acceptable or not based on a landing error below a threshold of 0.2 meters.

As depicted in Fig. 10, the computed feasible region illustrates the performance of the robot across the tested positions. A key observation is the symmetry of performance with respect to the X-axis, which reflects the symmetrical configuration of the robot’s legs. This symmetry confirms that the robot achieves consistent jumping accuracy for lateral displacements, with no noticeable difference between rightward and leftward jumps. Although the jumps in the backward direction were not tested over long distances, the results suggest similar performance to frontward jumps. The logarithmic color scale used in the figure emphasizes the subtle differences in landing precision, highlighting that the robot’s best performance is within the 0.5-meter radius from the origin, where it achieves exceptional accuracy. Landing errors in this range are consistently below 5 cm, showcasing the high precision and of the learned policy for short to medium-range jumps. To gain a clearer understanding of the robot’s behavior during longer jumps, Fig. 11 presents a comparison between the target and actual distances achieved by the robot for both front (left plot) and back jumps (right plot). In an ideal scenario, the robot’s actual jump distances would align perfectly with the desired target, depicted by the dashed diagonal line in the plot. The green shaded area corresponds to jumps executed without any collisions involving non-foot parts of the robot, representing the actual performance of the policy. The red samples are jumps that are failing. For target distances

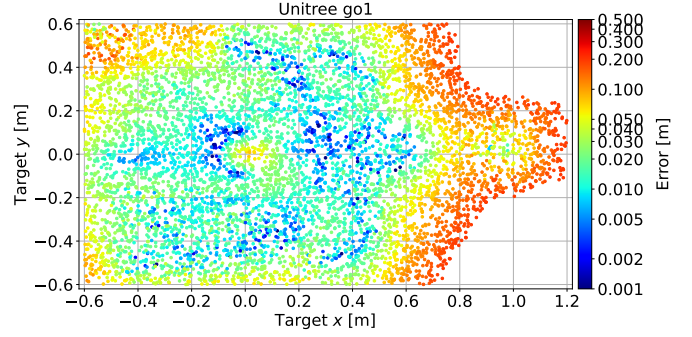


Fig. 10: Feasible region for flat omni-directional jumps (without change in orientation) for the Go1 robot: set of targets with landing error below 0.2 m.

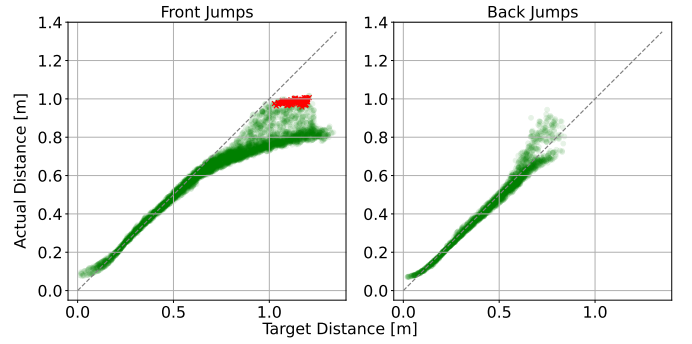


Fig. 11: In green, target vs actual jump distance for both front (left plot) and back (right plot) jumps using the *omni-directional* jump policy with the Go1 robot. Jump failures are highlighted in red.

up to 0.6 meters, the policy performs well, showing precise and consistent jumps indicating that the robot effectively tracks the desired trajectory. The relatively narrow distribution of points in this range indicates that the robot maintains good accuracy as the target distance varies within this limit. However, as the target distance exceeds 0.6 meters, the policy exhibits more cautious behavior. This conservatism is reflected in the robot’s inability to execute larger jumps beyond this distance.

This suggests that the policy prioritizes feasibility and safety over maximizing jump distance, aiming to ensure stable landings and minimize the risk of failure and is consistent with the trend observed in the reward plot, where minimal violations of constraints were recorded. Rather than pushing the system toward potentially unsafe physical limits, it favours reliability and consistency. Introducing a NN focused on improving landing proficiency is expected to significantly enhance performance, particularly by enabling longer jumps. This is because rebound effects will be handled by the dedicated landing policy, rather than requiring the jump policy to adopt a conservative approach. Finally, there are 124 failure points around the 1-meter jump distance, equivalent to only the 1% of the jumps.

2) *Upward and Downward Jumps:* In this subsection, we evaluate the performance of the learned policy in executing jumps involving both positive and negative vertical displacements, therefore focusing on upward and downward jumps. These types of jumps are critical for robotic navigation on

uneven terrains or in environments with varying surface elevations, where the ability to adapt to different heights is essential for effective mobility, and are mostly overlooked in the literature. The tests were conducted within the samples in the test region as before, but with target locations where Z component was set to different values along the z-axis. These ranged from upward jumps to higher platforms (positive vertical displacement) to downward jumps onto lower surfaces (negative vertical displacement). For each target location (x,y), the maximum/minimum achievable height is recorded. The results of these tests were used to generate height maps (see Fig. 12) for upward (left) and downward jumps (right), respectively.

As shown in the left contour plot, the robot is capable of executing jumps to surfaces with up to 0.26 meters of vertical displacement. The total range of successful upward jumps lies between 0.16 meters and 0.28 meters, with some variation depending on the lateral displacement. Notably, the robot tends to struggle with upward jumps targeting locations in the back region, particularly when combined with significant lateral displacement. This behavior is expected due to the kinematic constraints of the robot in these specific configurations, where the required force distribution for pushing off is less efficient (given the leg shape), and the available range of motion becomes more limited.

In contrast, the right contour plot demonstrates that the robot can successfully perform downward jumps across its entire feasible region, with vertical displacements up to -0.4 meters, which aligns with the bounds established during the training and test phase. This indicates that the robot could possibly handle even larger drops. The greater effectiveness in downward jumps can be attributed to the assistance of gravity in achieving the target, making the kinematic demands less stringent compared to upward jumps.

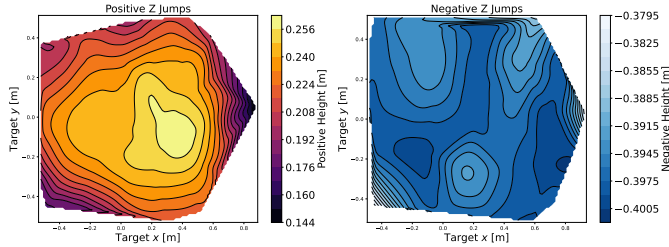


Fig. 12: Height map for both upward jumps (on the left) and downward jumps (on the right) for the Go1 robot.

3) *In-place Rotation Jumps*: In this test, we performed a series of in-place jumps where each jump involved a different target orientation change for the yaw component. This capability is particularly beneficial for executing maneuvers that require quick rotations, such as twist jumps or adjustments to prepare for subsequent locomotion. The test examines whether the learned policy can effectively control the robot's orientation ensuring it reaches the desired landing position with a specified orientation. The polar plot in Fig. 13 shows the variation of the landing orientation error (radius) as a function of the desired yaw angle. In-place jumps with no orientation change (origin of the polar plot) serve as a baseline, resulting

in minimal orientation error, as expected. However, as the desired yaw angle increases in magnitude (both positively and negatively) the orientation error raises symmetrically. This symmetric behavior reflects the robot's ability to handle yaw rotations in either direction.

The maximum observed yaw error is approximately 6 degrees, which is a satisfactory result, considering that it stays under 10% of the desired yaw angle across a wide range of rotations. This level of error indicates that the learned policy is proficient at managing dynamic jumps involving significant reorientation, maintaining a reasonable level of accuracy even under challenging angular displacement scenarios.

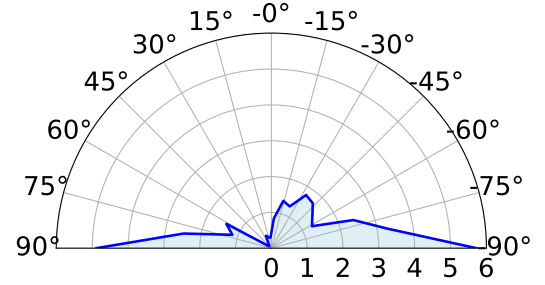


Fig. 13: Polar plot of the landing orientation error (radius) vs the desired yaw angle, both expressed in degrees for the Go1 robot.

D. Sim-to-sim evaluation and robustness to parameter variation

In this section, we will test the trained policy using a simulation framework (Locosim [45] based on Gazebo) different than the one used for training (Orbit). Our intent is twofold: 1) assess the impact of the sim-to-sim gap by evaluating how different simulation environments affect robot behavior and performance; 2) systematically study how changes in physical parameters—such as mass distribution and joint friction affect the robot's dynamic behavior, with a specific focus on the accuracy and reliability of jumping maneuvers. To this extent we consider two types of jumps on flat terrain: a forward jump of 0.4 m (*FWD*) and a composite diagonal jump (*DIAG*) with target $c_{tg,x} = 0.3$ m, $c_{tg,y} = 0.2$ m, $\psi_{tg} = 45$ deg; 3 types of tests: *NOM* (no parametric variation), *DV* (variations on joint damping) and *MV* (variations on mass); and two robot platforms (Go1, Aliengo). We performed 100 simulations for each tuple (robot, jump type, test). For the cases **DV** and **MV** with parametric variations sampled from a continuous uniform distribution $\mathcal{U}(0, 1)$ as follows:

$$\begin{aligned} m_{\text{var}} &= m_0 + \underbrace{m_0 p}_{\Delta m_{\text{max}}} \mathcal{U}(-1, 1) \\ d_{\text{var}} &= d_{\text{max}} \cdot \mathcal{U}(0, 1) \end{aligned} \quad (28)$$

Here, m_0 is the default mass, $p = 0.5$ is the perturbation percentage, and m_{var} and d_{var} are the modified mass and damping, respectively, (the default damping being 0). Then, for

each tuple, we computed the mean and the standard deviation of the errors on the landing position e_x , e_y and orientation e_ψ as reported in Table VI.

TABLE VI
Statistics of accuracy VS parameter uncertainty

#	Robot	Jump Type	Test	e_x	e_y	e_ψ
T1	Go1	FWD	NOM	0.013 ± 0.002	X	X
T2	Go1	FWD	DV	0.059 ± 0.023	X	X
T3	Go1	FWD	MV	0.014 ± 0.007	X	X
T4	Go1	DIAG	NOM	0.019 ± 0.000	-0.024 ± 0.001	1.523 ± 0.128
T5	Go1	DIAG	DV	0.032 ± 0.011	-0.003 ± 0.012	3.982 ± 2.237
T6	Go1	DIAG	MV	0.019 ± 0.001	-0.023 ± 0.005	1.632 ± 1.137
T7	Aliengo	FWD	NOM	0.010 ± 0.017	X	X
T8	Aliengo	FWD	DV	0.044 ± 0.024	X	X
T9	Aliengo	FWD	MV	0.014 ± 0.024	X	X
T10	Aliengo	DIAG	NOM	0.005 ± 0.013	-0.005 ± 0.028	10.992 ± 2.871
T11	Aliengo	DIAG	DV	0.028 ± 0.015	0.020 ± 0.024	9.166 ± 3.577
T12	Aliengo	DIAG	MV	0.009 ± 0.016	0.003 ± 0.030	11.304 ± 3.520

Inspecting the values for the nominal test (T1 and T4) we can observe a good matching for a *FWD* jump (see Fig. 10) in terms of the position error (≈ 1.3 cm) and for a *DIAG* jump (see Fig. 13) in terms of the orientation error (1.5 deg) demonstrating a low sim-to-sim gap. Regarding the tests involving changes in dynamic parameters of the robot there is a very little influence of the mass (despite its variation is up to 50%) while a higher influence is observed for the damping with the position error in the *FWD* jump which is increasing from 1.5 cm (T1) to 5.9 cm (T2), which is, in percentage, still below the 15% of the whole jump length. These results are particularly relevant for the *MV* test, where gravity compensation was computed using the default mass value, resulting in a significant deviation from real conditions, showing that leveraging a low-level controllee, our method exhibits good robustness to parameter uncertainty without the need to add *domain randomization* during the training. Similar results are observed on the orientation error that remains between 1.5 and 4 degrees in the case of *DIAG* jump (T4 and T5). Equivalent outcomes were obtained with the Aliengo robot (for which the policy was specifically retrained) with a maximum landing error for a *FWD* jump of 4.4 cm in the case of *DV* (T8) with respect to 1 cm of the *NOM* (T7).

E. Joint Feasibility of the Learned Trajectory

In this Section we want to assess both the quality of the tracking of the generated trajectory and their physical feasibility considering constraints on joint position, velocity and torque. Fig. 14 presents the desired and actual trajectories for CoM position, velocity, yaw, and yaw rate during a composite *DIAG* jump with the Go1 robot in a simulation with Locosim, being the *DIAG* jump a good template to evaluate tracking performance because it involves motion along multiple directions. The tracking is good during the whole thrusting phase which is highlighted by the shaded area. Accurate tracking of joint positions and velocities further demonstrates the controller's ability to maintain stability throughout the jump. Additionally, in the accompanying video (figure not included here due to space constraints) we assess whether any kinematic, velocity, or torque limit is exceeded. As shown, the system consistently operates within all joint limits during

the thrust phase indicating that, even under demanding conditions, the policy respects the robot's physical constraints. This physical compliance results in a conservative behavior, particularly evident in longer-distance jumps, where the policy prioritizes safety (c.f Section V-F). Overall, the results confirm the method's physical feasibility, whose success is largely due to the integration of domain knowledge into the reward design.

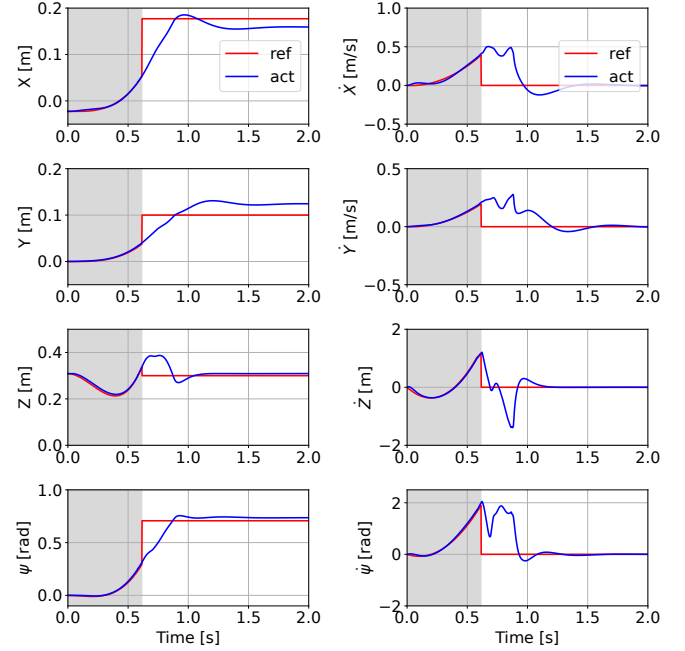


Fig. 14: *Simulation*. Tracking performances for the *DIAG* jump with the Go1 robot: CoM position tracking (upper-left plots) and orientation (yaw) tracking (lower-left plot). (right) tracking of CoM velocity (upper-right plots) and of the yaw rate (lower-right plot). References are in red and are switched to target values after lift-off, the actual measurements are in blue. The shaded area highlights the thrust phase.

F. Comparison with SOA Approach

In this section we compare our method with the state-of-the-art E2E approach developed by Atanassov et al. [39], which is currently regarded as the benchmark for RL-based jumping, offering a valuable reference for evaluating our performance. Briefly, their method involves dividing the learning process into three curriculum stages, with the same policy, represented by a neural network, being refined sequentially. The first stage focuses on in-place jumps with variable positive height displacements. The second stage introduces forward and lateral displacement jumps, while the final stage involves obstacle-aware jumps, where the robot learns to jump onto a given obstacle. The work was developed using an early version of Isaac-Gym in combination with a predecessor framework of Orbit, and the total training time took approximately 10 hours. Like our work, their training utilized parallelization with 4096 simulated robots running simultaneously. However, in their case, each policy update was computed after 24 environment steps, resulting in a higher data requirement compared

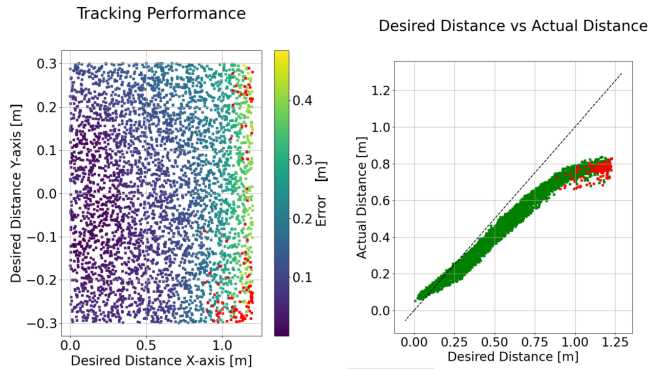


Fig. 15: Tracking performances reported in Atassanov et al. [39], with a policy trained for solely forward jumps. Unsuccessful jumps are depicted in red.

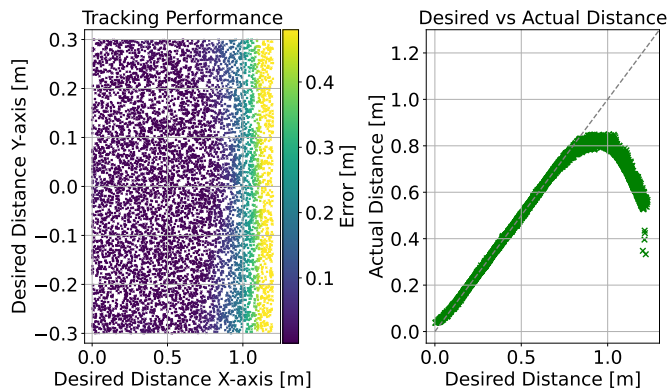


Fig. 16: Tracking performances for the Go1 robot reported for our approach with a policy trained for solely forward jumps.

to our method. The entire training process required 23000 iterations, with 3000 iterations for the first stage and 10000 for each of the remaining two stages. This highlights the high data requirements of E2E approaches compared to our more sample-efficient GRL method that converges after only 2000 training steps (Fig. 9). In Fig. 15, we present the results of their approach for a policy trained specifically for forward jumps with the Go1 robot, while in Fig. 16, we show our results with our policy using a similar form factor for equal comparison. For consistency, we retrained our policy for forward jumps by utilizing their training flat region composed of an X-range of (0-1.2) meters and a Y-range of (-0.3, 0.3) meters. A key observation is that, in their approach, distant jumps combined with lateral displacements often result in failed jumps due to improper contacts that are not made by the feet. In contrast, our approach avoids such failures by ensuring the respect of system constraints also in the task space, featuring the same maximum jump distance compared to their method but with a more *uniform* performance within the previously defined feasible region, as evidenced by the proximity of our jump distributions to the ideal jumping behavior (diagonal line). Although their plot does not explicitly report jump heights, in the paper they declare that their method was tested with jump heights of only 0.05 and 0.1 meters, whereas our method demonstrated the ability to reach up to 0.26 meters for forward jumps. This highlights our method’s superior capability for

handling higher vertical displacements. Note that with respect to the omnidirectional policy, where the maximum accurate landing was limited to 0.6 m, with the forward policy we are able to attain longer jumps up to 0.8 m.

To summarize, our method outperforms Atanassov’s in several aspects: (1) it delivers higher accuracy, as seen in the left plot, where the region with less than 10 cm error extends uniformly along the Y-axis up to 80 cm jumps; (2) this accuracy is also reflected in the right plot, where samples are more tightly distributed around the ideal line; (3) it enables higher elevations; (4) the jump trajectory can be verified before the execution. Finally, unlike the omni-directional jump policy, our method produces no failures (i.e., no red samples). Our method adopts a more conservative strategy that prioritizes safety and accuracy, with the added advantage of requiring significantly fewer samples and avoiding complex multi-stage reward engineering. This makes our approach not only more data-efficient but also more straightforward to implement and train, without sacrificing real-world feasibility and performance. This is supported by the evidence that their approach incorporates 25 distinct reward terms tailored to each curriculum stage. In contrast, our approach uses only 15 reward terms and a single-stage learning.

G. Zero-Shot on Different Robotic Platform

To demonstrate the generalization of our approach, we selected a quadruped platform similar to the Go1 and performed a zero-shot jump with this platform, making only the necessary low-level control adjustments. The selected platform is the Unitree Aliengo, which weighs approximately 24 kg and features longer leg links with higher torque limits compared to the Go1. As shown in the accompanying video, we tested on Aliengo a forward jump of 0.6 m employing the policy trained on Go1, achieving a landing error of 0.1 m while satisfying all system constraints related to the robot’s characteristics. This underscores the potential for directly applying the trained policy to robotic systems with similar specifications, or alternatively, for rapidly fine-tuning the pre-trained policy (without retraining from scratch) to adapt to differences in actuation, mass, and dimensional characteristics across platforms. By defining both the action space and observation space in task-space, our approach contributes to making the policy largely independent of the specific robotic platform.

H. Experiments with the real quadruped

In this section, we report real experiments of the *FWD*, *BWD* and *DIAG* jumps performed both with the Aliengo and Go1 robots. *BWD* jump is a 40 cm jump backwards. The experiments were repeated 10 times for each jump type and are shown in the accompanying video. The estimation of the CoM position is implemented by leg odometry assuming that the feet remain in stance during the whole thrust while the orientation comes from Inertial Measurement Unit (IMU) readings. We measured the landing location with a measurement tape because the odometry would provide non-meaningful estimates after lift-off, and a Motion Capture System was not available. Because of the short duration of the jump and

the high acceleration involved, it was impossible to estimate the *apex* and *touchdown* conditions (as customary done in robotics) via contact force estimation or contact switches. In the first case, it was difficult to set a fixed threshold on the ground reaction forces to assess the contact condition because the high joint acceleration due to the leg retraction created fictitious force estimation that triggered early touchdown when the robot was still in the air. In the second case, the contact sensor in the Unitree robot was unacceptably slow ($\approx 100\text{ms}$) in detecting the lift-off, because it is based on air pressure sensors, which are inherently subject to pressure dynamics.

The key to achieve successful experiments was leveraging our physically informed action parametrization to *heuristically* estimate the apex and touchdown instants by using ballistic equations (see Section V-B). We report in Table VII the statistics (mean and std. deviation) of the position error (in the x direction) and orientation errors (in yaw direction) for the three types of jumps (performing 10 experiments for each), with the Aliengo robot. We report also the *FWD* jump with the Go1 robot, for comparison. The mean error for the *FWD* jump

TABLE VII
Statistics of accuracy in real experiments

ID	Robot	Jump Type	$e_x[m]$	$e_y[m]$	$e_\psi[\text{rad}]$
T1	Aliengo	FWD	0.046 ± 0.01	N/A	N/A
T2	Aliengo	BWD	0.071 ± 0.015	N/A	N/A
T3	Aliengo	DIAG	-0.057 ± 0.017	-0.16 ± 0.026	-12.17 ± 3.1
T4	Go1	FWD	0.01 ± 0.017	N/A	N/A

with the Go1 robot is quite close to the simulation value (T4) (c.f. Table VI) but more than three times higher for the Aliengo robot (T1) with the robot undershooting the target. Conversely, by analyzing the error direction in *BWD* jumps, the Aliengo robot tends to overshoot the target. Regarding the composite *DIAG* jump, the robot overshoots the target too in the 3 directions, resulting, for orientation, in a mean error of around -12 deg, which is 26% of the target 45-degree orientation. Despite the fact that the error offsets are not negligible, the reader should note that their standard deviation is low, which showcases the high reliability of the approach in terms of high repeatability. We believe the source of these errors is due to friction which has not been properly compensated. The bad tracking on the y direction is responsible for the 16 cm average error that we obtain in that direction. Training an actuator NN [20] can be effective in removing these non-idealities from the low-level controller. We also showcase the feasibility of the generated reference trajectories checking the tracking performances in Fig. 17 for the *DIAG* jump. Solely the thrust phase is reported because the odometry would provide non-meaningful results after lift-off. We can observe that the tracking is reasonable at the position level (left plot) and good at the velocity level (right plots), both for CoM and base orientation. Being the lift-off velocity crucial for most of the landing accuracy.

VI. CONCLUSIONS

In this work, we propose a novel approach for generating jump manoeuvres in legged robots. The methodology centres on the notion of Guided Reinforcement Learning, which we

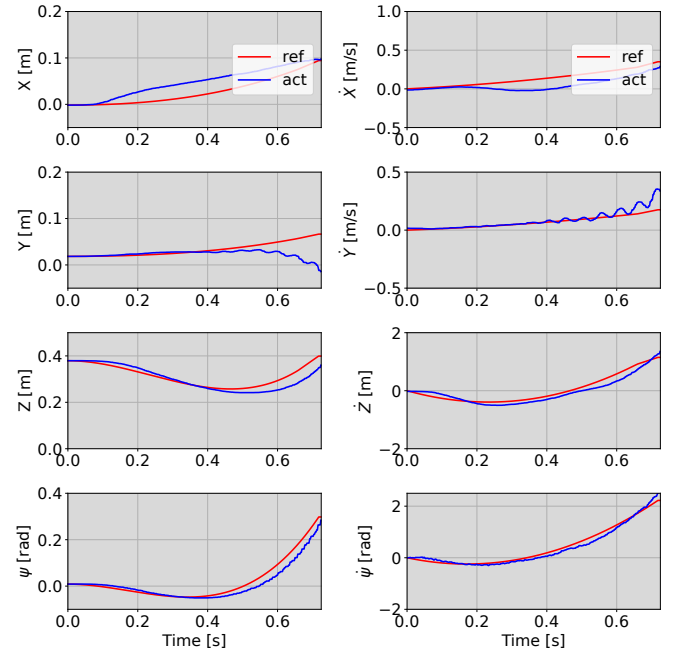


Fig. 17: *Experiments*. Tracking performances during the *thrust* phase, for the *DIAG* jump with the Aliengo robot: CoM position tracking (first 3 plots-left) and orientation (yaw) tracking (lower-left plot). The CoM velocity is shown in the upper-right plots whilst the yaw rate in the lower-right plot. References are in red while actual measurements are in blue.

interpret as the injection of physical intuition into the learning process.

In particular, we use a geometric parametrisation of the curve followed by the centre of mass during the thrust phase, and concentrate the learning process into a small set of parameters—achieving greater sample-efficiency and reduced computation time compared to customary E2E approaches. We also employ classical control to track the generated trajectory at the joint level, resulting in a good degree of robustness to parameter uncertainty. Orientation is managed via a separate trajectory, a solution that enables complex and dynamic manoeuvres such as in-place twist jumps for rapid changes in heading. The learned policy shows a remarkable ability to handle jumps of varying heights—including downward jumps—and to perform pure yaw rotations. The generated trajectories successfully manage orientation changes while consistently respecting the system’s physical constraints.

Contrary to previous approaches [46] in which morphology and control strategy are tightly bound, we have achieved a good degree of platform independence. A crucial choice to obtain this result was excluding joint-level information from observations and formulating actions directly in task space, which allowed us to manage the differences between the platforms by simply using inverse kinematics. As a direct validation of this idea, we were able to demonstrate zero-shot transfer of the policy learned for the Go1 robot to the Aliengo platform.

Compared to state-of-the-art end-to-end reinforcement learning approaches [39], our method achieves comparable

performance on jump tasks while requiring significantly less training—only 2,000 episodes versus millions—marking a substantial improvement in training efficiency. This gain in efficiency does not come at the expense of performance: both the accuracy of the jumps and the achieved elevation outperform the baseline [39].

In spite of the evident success of the application of GRL to the challenging task of managing robot jumps, several limitations remain that will require future research efforts. Some of the most important are the following:

- 1) The current method is purely kinematic. We believe that controlling the dynamics in torque-controlled systems would produce significant performance improvements.
- 2) The policy has been trained assuming zero initial velocity, which restricts its application in dynamic scenarios such as multiple jumping tasks. Generalising to arbitrary initial velocities will be an obvious research direction for future work.
- 3) We are seeking to extend the state representation to include the position of the feet relative to the base frame. This improvement would enable operations in adverse environments, such as sloped surfaces.
- 4) Including a $\Delta\tau$ -network, trained via an E2E approach, could allow us to adjust the joint configuration at each time step and support airborne reorientation, helping to mitigate the impact during the landing phase.
- 5) We plan to increase the sample efficiency and performance of our method even further by considering data augmentation techniques that exploit the symmetries of the quadruped robot and the task [47, 48].
- 6) Considering training scenarios where the robot rears on two legs could lead to more dynamic pre-jump strategies and expand the action repertoire. Obvious benefits in terms of robustness and generality could be achieved by including deformable terrain—such as trampolines or soft ground—within the training environment.
- 7) Finally, we aim to investigate the integration of reinforcement learning with numerical optimisation techniques, to combine the flexibility of data-driven methods with the precision and interpretability of model-based approaches.

FUNDING DECLARATION

This research received no specific grant from any funding agency in the public, commercial, or not-for-profit sectors.

APPENDIX A DERIVATIVE OF A BÉZIER FUNCTION

Lemma A.1. *The derivative of a Bézier curve $\mathbf{B}(t) = \sum_{i=0}^n b_i^n(t) \mathbf{P}_i$ of degree n is a Bézier curve of order $n-1$ of the form [49]:*

$$\dot{\mathbf{B}}(t) = \sum_{i=0}^{n-1} b_i^{n-1}(t) \mathbf{P}'_i \quad 0 \leq t \leq 1 \quad (29)$$

with control points defined as

$$\mathbf{P}'_i = n(\mathbf{P}_{i+1} - \mathbf{P}_i) \quad (30)$$

Proof. To calculate the derivative of $\mathbf{B}(t)$, we begin by noting that since the control points \mathbf{P}_i are constant and independent of time t , the calculation simplifies to differentiating the Bernstein basis polynomials,

$$\dot{\mathbf{B}}(t) = \sum_{i=0}^n \mathbf{P}_i \frac{db_i^n}{dt}(t) \quad (31)$$

where it can be proved that the derivative can be written as a combination of two polynomials of lower degree:

$$\frac{db_i^n}{dt}(t) = \dot{b}_i^n(t) = n(b_{i-1}^{n-1}(t) - b_i^{n-1}(t)) \quad (32)$$

Hence, we can then compute the derivative of the curve obtaining:

$$\dot{\mathbf{B}}(t) = \sum_{i=0}^n \mathbf{P}_i n [b_{i-1}^{n-1}(t) - b_i^{n-1}(t)] \quad (33)$$

With the convention $b_{-1}^{n-1} = b_n^{n-1} = 0$ that comes from the fact the binomial coefficients in the Bernstein Polynomials vanish outside their natural range. Splitting and regrouping the sums we get

$$\dot{\mathbf{B}}(t) = n \left[\sum_{i=0}^n \mathbf{P}_i b_{i-1}^{n-1}(t) - \sum_{i=0}^n \mathbf{P}_i b_i^{n-1}(t) \right] \quad (34)$$

Now shifting the index in the first sum (i.e. let $j = i - 1$) and considering $b_{-1}^{n-1} = 0$:

$$\sum_{i=0}^n \mathbf{P}_i b_{i-1}^{n-1}(t) = \sum_{j=-1}^{n-1} \mathbf{P}_{j+1} b_j^{n-1}(t) = \sum_{j=0}^{n-1} \mathbf{P}_{j+1} b_j^{n-1}(t) \quad (35)$$

a similar argument can be followed for the second term in the sum using $b_n^{n-1} = 0$. Then, putting all together:

$$\begin{aligned} \dot{\mathbf{B}}(t) &= n \left[\sum_{i=0}^{n-1} \mathbf{P}_{i+1} b_i^{n-1}(t) - \sum_{i=0}^{n-1} \mathbf{P}_i b_i^{n-1}(t) \right] \\ &= n \sum_{i=0}^{n-1} (\mathbf{P}_{i+1} - \mathbf{P}_i) b_i^{n-1} \end{aligned} \quad (36)$$

□

APPENDIX B EXPLICIT FORM OF A CUBIC BÉZIER CURVE

For clarity in notation, we will define the normalized time \hat{t} as follows:

$$\hat{t} = \frac{t}{T_{th}} \quad 0 \leq t \leq T_{th} \quad (37)$$

The explicit forms for both the cubic Bézier curve and its corresponding quadratic derivative (computed from (36)) are as follows:

$$\begin{aligned} \mathbf{B}(t) &= (1 - \hat{t})^3 \mathbf{P}_0 + 3(1 - \hat{t})^2 \hat{t} \mathbf{P}_1 + 3(1 - \hat{t}) \hat{t}^2 \mathbf{P}_2 + \hat{t}^3 \mathbf{P}_3 \\ \dot{\mathbf{B}}(t) &= \frac{3}{T_{th}} (1 - \hat{t})^2 (\mathbf{P}_1 - \mathbf{P}_0) + \frac{6}{T_{th}} (1 - \hat{t}) \hat{t} (\mathbf{P}_2 - \mathbf{P}_1) \\ &\quad + \frac{3}{T_{th}} \hat{t}^2 (\mathbf{P}_3 - \mathbf{P}_2) \\ &= (1 - \hat{t})^2 \mathbf{P}'_0 + 2(1 - \hat{t}) \hat{t} \mathbf{P}'_1 + \hat{t}^2 \mathbf{P}'_2 \end{aligned} \quad (38)$$

REFERENCES

- [1] L. Amatiucci, G. Turrissi, A. Bratta, V. Barasuol, and C. Semini, "Vero: A vacuum-cleaner-equipped quadruped robot for efficient litter removal," *Journal of Field Robotics*, vol. 41, no. 6, p. 1829–1842, 2024.
- [2] P. Biswal and P. K. Mohanty, "Development of quadruped walking robots: A review," *Ain Shams Engineering Journal*, vol. 12, no. 2, pp. 2017–2031, 2021.
- [3] F. Jenelten, R. Grandia, F. Farshidian, and M. Hutter, "Tamols: Terrain-aware motion optimization for legged systems," *IEEE Transactions on Robotics*, vol. 38, no. 6, pp. 3395–3413, 2022.
- [4] F. Roscia, M. Focchi, A. D. Prete, D. G. Caldwell, and C. Semini, "Reactive landing controller for quadruped robots," *IEEE Robotics and Automation Letters*, vol. 8, no. 11, pp. 7210–7217, 2023.
- [5] H.-W. Park, P. M. Wensing, and S. Kim, "High-speed bounding with the mit cheetah 2: Control design and experiments," *The International Journal of Robotics Research*, vol. 36, no. 2, pp. 167–192, 2017.
- [6] J. K. Yim, B. R. P. Singh, E. K. Wang, R. Featherstone, and R. S. Fearing, "Precision robotic leaping and landing using stance-phase balance," *IEEE Robotics and Automation Letters*, vol. 5, no. 2, pp. 3422–3429, 2020.
- [7] C. Nguyen and Q. Nguyen, "Contact-timing and trajectory optimization for 3d jumping on quadruped robots," in *2022 IEEE/RSJ International Conference on Intelligent Robots and Systems (IROS)*, 2022, pp. 11 994–11 999.
- [8] B. Katz, J. Di Carlo, and S. Kim, "Mini cheetah: A platform for pushing the limits of dynamic quadruped control," in *2019 international conference on robotics and automation (ICRA)*. IEEE, 2019, pp. 6295–6301.
- [9] M. Chignoli and S. Kim, "Online trajectory optimization for dynamic aerial motions of a quadruped robot," in *2021 IEEE International Conference on Robotics and Automation (ICRA)*. IEEE, 2021, pp. 7693–7699.
- [10] G. García, R. Griffin, and J. Pratt, "Time-varying model predictive control for highly dynamic motions of quadrupedal robots," in *2021 IEEE International Conference on Robotics and Automation (ICRA)*, 2021, pp. 7344–7349.
- [11] M. Chignoli, S. Morozov, and S. Kim, "Rapid and reliable quadruped motion planning with omnidirectional jumping," in *2022 International Conference on Robotics and Automation (ICRA)*, 2022, pp. 6621–6627.
- [12] Z. Song, L. Yue, G. Sun, Y. Ling, H. Wei, L. Gui, and Y.-H. Liu, "An optimal motion planning framework for quadruped jumping," in *2022 IEEE/RSJ International Conference on Intelligent Robots and Systems (IROS)*, 2022, pp. 11 366–11 373.
- [13] H. Li and P. M. Wensing, "Cafe-mpc: A cascaded-fidelity model predictive control framework with tuning-free whole-body control," *IEEE Transactions on Robotics*, vol. 41, pp. 837–856, 2025.
- [14] J. Ding, V. Atanassov, E. Panichi, J. Kober, and C. Della Santina, "Robust quadrupedal jumping with impact-aware landing: Exploiting parallel elasticity," *IEEE Transactions on Robotics*, 2024.
- [15] C. Mastalli, W. Merkt, G. Xin, J. Shim, M. Mistry, I. Havoutis, and S. Vijayakumar, "Agile maneuvers in legged robots: a predictive control approach," *ArXiv*, 2022.
- [16] H. Li and P. M. Wensing, "Cafe-mpc: A cascaded-fidelity model predictive control framework with tuning-free whole-body control," 2024.
- [17] G. Bellegarda, M. Shafiee, M. E. Özberk, and A. Ijspeert, "Quadruped-frog: Rapid online optimization of continuous quadruped jumping," *arXiv preprint arXiv:2403.06954*, 2024.
- [18] T. P. Lillicrap, J. J. Hunt, A. Pritzel, N. M. O. Heess, T. Erez, Y. Tassa, D. Silver, and D. Wierstra, "Continuous control with deep reinforcement learning," *CoRR*, vol. abs/1509.02971, 2015.
- [19] C. Gehring, S. Coros, M. Hutter, C. D. Bellicoso, H. Heijnen, R. Diethelm, M. Bloesch, P. Fankhauser, J. Hwangbo, M. Hoepflinger, *et al.*, "Practice makes perfect: An optimization-based approach to controlling agile motions for a quadruped robot," *IEEE Robotics & Automation Magazine*, vol. 23, no. 1, pp. 34–43, 2016.
- [20] J. Hwangbo, J. Lee, A. Dosovitskiy, D. Bellicoso, V. Tsounis, V. Koltun, and M. Hutter, "Learning agile and dynamic motor skills for legged robots," *Science Robotics*, vol. 4, no. 26, p. eaau5872, 2019.
- [21] X. Peng, E. Coumans, T. Zhang, T.-W. Lee, J. Tan, and S. Levine, "Learning agile robotic locomotion skills by imitating animals," *Robotics: Science and Systems*, 07 2020.
- [22] G. Ji, J. Mun, H. Kim, and J. Hwangbo, "Concurrent training of a control policy and a state estimator for dynamic and robust legged locomotion," *IEEE Robotics and Automation Letters*, vol. 7, no. 2, pp. 4630–4637, 2022.
- [23] N. Rudin, D. Hoeller, P. Reist, and M. Hutter, "Learning to walk in minutes using massively parallel deep reinforcement learning," in *Conference on Robot Learning*. PMLR, 2022, pp. 91–100.
- [24] P. Fankhauser, M. Hutter, C. Gehring, M. Bloesch, M. A. Hoepflinger, and R. Siegwart, "Reinforcement learning of single legged locomotion," in *2013 IEEE/RSJ International Conference on Intelligent Robots and Systems*. IEEE, 2013, pp. 188–193.
- [25] D. Hoeller, N. Rudin, D. Sako, and M. Hutter, "Anymal parkour: Learning agile navigation for quadrupedal robots," *Science Robotics*, vol. 9, no. 88, p. eadi7566, 2024.
- [26] I. OpenAI, "Benchmarks for spinning up implementations," 2022, <https://spinningup.openai.com/en/latest/spinningup/bench.html#benchmarks-for-spinning-up-implementations> [Accessed: 26/02/2023].
- [27] Y. Yang, X. Meng, W. Yu, T. Zhang, J. Tan, and B. Boots, "Continuous versatile jumping using learned action residuals," in *Proceedings of The 5th Annual Learning for Dynamics and Control Conference*, ser. Proceedings of Machine Learning Research, N. Matni, M. Morari, and G. J. Pappas, Eds., vol. 211. PMLR, 15–16 Jun 2023, pp. 770–782.
- [28] A. Y. Majid, S. Saaybi, T. van Rietbergen, V. François-Lavet, R. V. Prasad, and C. Verhoeven, "Deep reinforcement learning versus evolution strategies: A comparative survey," *ArXiv*, vol. abs/2110.01411, 2021.
- [29] M. Bogdanovic, M. Khadiv, and L. Righetti, "Model-free reinforcement learning for robust locomotion using demonstrations from trajectory optimization," *Frontiers in Robotics and AI*, vol. 9, p. 854212, 2022.
- [30] G. Bellegarda, C. Nguyen, and Q. Nguyen, "Robust quadruped jumping via deep reinforcement learning," 2023.
- [31] G. Grandesso, E. Alboni, G. P. R. Papini, P. M. Wensing, and A. Del Prete, "Cacto: Continuous actor-critic with trajectory optimization—towards global optimality," *IEEE Robotics and Automation Letters*, vol. 8, no. 6, pp. 3318–3325, 2023.
- [32] X. B. Peng and M. van de Panne, "Learning locomotion skills using deeprl: Does the choice of action space matter?" in *Proc. ACM SIGGRAPH / Eurographics Symposium on Computer Animation*, 2017.
- [33] G. Bellegarda and K. Byl, "Training in task space to speed up and guide reinforcement learning," in *2019 IEEE/RSJ International Conference on Intelligent Robots and Systems (IROS)*, 2019, pp. 2693–2699.
- [34] S. Chen, B. Zhang, M. W. Mueller, A. Rai, and K. Sreenath, "Learning torque control for quadrupedal locomotion," in *2023 IEEE-RAS 22nd International Conference on Humanoid Robots (Humanoids)*. IEEE, 2023, pp. 1–8.
- [35] M. Aractingi, P.-A. Léziart, T. Flayols, J. Perez, T. Silander, and P. Souères, "Controlling the solo12 quadruped robot with deep reinforcement learning," *scientific Reports*, vol. 13, no. 1, p. 11945, 2023.
- [36] M. Shafiee, G. Bellegarda, and A. Ijspeert, "Manyquadrupeds:

- Learning a single locomotion policy for diverse quadruped robots,” in *2024 IEEE International Conference on Robotics and Automation (ICRA)*. IEEE, 2024, pp. 3471–3477.
- [37] Y. Yang, X. Meng, W. Yu, T. Zhang, J. Tan, and B. Boots, “Continuous versatile jumping using learned action residuals,” in *Proceedings of The 5th Annual Learning for Dynamics and Control Conference*, ser. Proceedings of Machine Learning Research, N. Matni, M. Morari, and G. J. Pappas, Eds., vol. 211. PMLR, 15–16 Jun 2023, pp. 770–782. [Online]. Available: <https://proceedings.mlr.press/v211/yang23b.html>
 - [38] F. Vezzi, J. Ding, A. Raffin, J. Kober, and C. Della Santina, “Two-stage learning of highly dynamic motions with rigid and articulated soft quadrupeds,” in *2024 IEEE International Conference on Robotics and Automation (ICRA)*. IEEE, 2024, pp. 9720–9726.
 - [39] V. Atanassov, J. Ding, J. Kober, I. Havoutis, and C. D. Santina, “Curriculum-based reinforcement learning for quadrupedal jumping: A reference-free design,” *IEEE Robotics & Automation Magazine*, pp. 2–15, 2024.
 - [40] J. Eßer, N. Bach, C. Jestel, O. Urbann, and S. Kerner, “Guided reinforcement learning: A review and evaluation for efficient and effective real-world robotics [survey],” *IEEE Robotics & Automation Magazine*, vol. 30, no. 2, pp. 67–85, 2022.
 - [41] R. Bussola, M. Focchi, A. Del Prete, D. Fontanelli, and L. Palopoli, “Efficient reinforcement learning for 3d jumping monopods,” *Sensors*, vol. 24, no. 15, p. 4981, 2024.
 - [42] J. Schulman, F. Wolski, P. Dhariwal, A. Radford, and O. Klimov, “Proximal policy optimization algorithms,” 2017.
 - [43] Y. Fujita and S.-i. Maeda, “Clipped action policy gradient,” in *International Conference on Machine Learning*. PMLR, 2018, pp. 1597–1606.
 - [44] M. Mittal, C. Yu, Q. Yu, J. Liu, N. Rudin, D. Hoeller, J. L. Yuan, R. Singh, Y. Guo, H. Mazhar, *et al.*, “Orbit: A unified simulation framework for interactive robot learning environments,” *IEEE Robotics and Automation Letters*, vol. 8, no. 6, pp. 3740–3747, 2023.
 - [45] M. Focchi, F. Roscia, and C. Semini, “Locosim: an open-source cross-platform robotics framework,” in *Climbing and Walking Robots Conference*. Springer, 2023, pp. 395–406.
 - [46] G. Feng, H. Zhang, Z. Li, X. B. Peng, B. Basireddy, L. Yue, Z. SONG, L. Yang, Y. Liu, K. Sreenath, and S. Levine, “Genloco: Generalized locomotion controllers for quadrupedal robots,” in *Proceedings of The 6th Conference on Robot Learning*, ser. Proceedings of Machine Learning Research, K. Liu, D. Kulic, and J. Ichnowski, Eds., vol. 205. PMLR, 14–18 Dec 2023, pp. 1893–1903. [Online]. Available: <https://proceedings.mlr.press/v205/feng23a.html>
 - [47] D. Ordoñez-Apaez, G. Turrissi, V. Kostic, M. Martin, A. Agudo, F. Moreno-Noguer, M. Pontil, C. Semini, and C. Mastalli, “Morphological symmetries in robotics,” *The International Journal of Robotics Research*, 2025.
 - [48] Z. Su, X. Huang, D. Ordoñez-Apaez, Y. Li, Z. Li, Q. Liao, G. Turrissi, M. Pontil, C. Semini, Y. Wu, and K. Sreenath, “Leveraging symmetry in rl-based legged locomotion control,” in *2024 IEEE/RSJ International Conference on Intelligent Robots and Systems (IROS)*, 2024, pp. 6899–6906.
 - [49] D. S. Greenstein, “Interpolation and approximation,” *SIAM Review*, vol. 7, no. 1, pp. 151–152, 1965.